Proposal for A Water Cherenkov Test Beam Experiment for Hyper-Kamiokande and Future Large-scale Water-based Detectors

R. Akutsu, P. de Perio, A. Konaka, T. Lindner, M. Pavin, and N. Prouse
TRIUMF, Vancouver, British Columbia, Canada

L. Anthony, P. Dunne, O. Jeremy, P. Jonsson, K. Long, M. Scott, Y. Uchida, and M. Wascko
Imperial College London, Department of Physics, London, United Kingdom

M. Barbi and N. Kolev
University of Regina, Department of Physics, Regina, Saskatchewan, Canada

V. Berardi and M.G. Catanesi
INFN Sezione di Bari and Università e Politecnico di Bari, Dipartimento Interuniversitario di Fisica, Bari, Italy

S. Bhadra and G. Santucci
York University, Department of Physics and Astronomy, Toronto, Ontario, Canada

D. Bhatkhande
Vishwakarma University, Kondhwa, Pune, India

S. Boyd and B. Richards
University of Warwick, Department of Physics, Coventry, United Kingdom

A. Bubak, J. Holeczek, J. Kisiel, and K. Porwit
University of Silesia, Institute of Physics, Katowice, Poland

A. Buchowicz, G. Galinski, A. Klekotko, R. Kurjata, J. Marzec,
W. Obrebski, G. Pastuszak, A. Rychter, K. Zaremba, and M. Ziembicki
Warsaw University of Technology, Institute of Radioelectronics and Multimedia Technology, Warsaw, Poland

M. Buizza Avanzini, O. Drapier, M. Gonin, T. Mueller, P. Paganini, and B. Quilain
Ecole Polytechnique, IN2P3-CNRS, Laboratoire Leprince-Ringuet, Palaiseau, France

A. Carroll, J. Coleman, P. Fernandez Menendez, N. McCauley, C. Metelko, and Y. Schnellbach
University of Liverpool, Department of Physics, Liverpool, United Kingdom

J. Chavez-Tabares, L. Falcon-Morales, J.A. Gonzalez, and A.K. Tomatani-Sánchez
Instituto Tecnologico de Estudios Superiores de Monterrey, Campus Guadalajara, México

J. Cederkall
Lund University, Department of Physics, Lund, Sweden

S.S. Chinchanikar, N.S. Deshmukh, C.S. Garde, S.V. Garode,[*] S.G. Joshi, A.P. Kulkarni, A.P. Kulkarni, and A.R. Mache
Vishwakarma Institute of Information Technology, Kondhwa, Pune, India

G. Collazuol, A. Longhin, and M. Mezzetto
INFN Sezione di Padova and Università di Padova, Dipartimento di Fisica, Padova, Italy

S. Cuen-Rochin
Instituto Tecnologico de Estudios Superiores de Monterrey, Campus Sinaloa, México and
Universidad Autónoma de Sinaloa, Culiacán, México

E. De la Fuente, B. Gonzalez-Alvarez, B. Navarro-Garcia, and F. Orozco-Luna
Universidad de Guadalajara, Guadalajara, México

G. De Rosa, C. Riccio, and A.C. Ruggeri
INFN Sezione di Napoli and Università di Napoli, Dipartimento di Fisica, Napoli, Italy

CERN-SPSC-2020-005 / SPSC-P-365
31/03/2021

T. Ekelof, K.E.I. Fransson, A. Miyazaki, M. Olvegård, E. O'Sullivan, and Y. Zou
Uppsala University, Department of Physics and Astronomy, Uppsala, Sweden

S. Fedotov, A. Khotjantsev, Y. Kudenko, O. Mineev, A. Shaykina, S. Suvorov, and N. Yershov
Institute for Nuclear Research of the Russian Academy of Sciences, Moscow, Russia

R. Gamboa Goñi
Universidad Panamericana, Campus Guadalajara, México

C. Giganti and M. Guigue
Sorbonne Université, Université Paris Diderot, CNRS/IN2P3, Laboratoire de Physique Nucléaire et de Hautes Energies (LPNHE), Paris, France

R. Gornea
Carleton University, Department of Physics, Ottawa, Canada and TRIUMF, Vancouver, British Columbia, Canada

M. Hartz
TRIUMF, Vancouver, British Columbia, Canada and Kavli Institute for the Physics and Mathematics of the Universe (WPI), The University of Tokyo Institutes for Advanced Study, University of Tokyo, Kashiwa, Chiba, Japan

A. Ioannisian
Yerevan Physics Institute, Yerevan, Armenia and Institute for Theoretical Physics and Modeling, Yerevan, Armenia

T. Ishida and T. Nakadaira
High Energy Accelerator Research Organization (KEK), Tsukuba, Ibaraki, Japan

M. Ishitsuka, M. Shinoki, and K. Yamauchi
Tokyo University of Science, Faculty of Science and Technology, Department of Physics, Noda, Chiba, Japan

B. Jamieson and J. Walker
University of Winnipeg, Department of Physics, Winnipeg, Manitoba, Canada

M. Jia, C. Vilela, and M.J. Wilking
State University of New York at Stony Brook, Department of Physics and Astronomy, Stony Brook, New York, U.S.A.

D. Karlen
University of Victoria, Department of Physics and Astronomy, Victoria, British Columbia, Canada and TRIUMF, Vancouver, British Columbia, Canada

U. Katz, J. Reubelt, and C. van Eldik
Friedrich Alexander University Erlangen-Nurnberg, Department of Physics, Erlangen, Germany

K. Kowalik, J. Lagoda, P. Mijakowski, E. Rondio, J. Zalipska, and G. Zarnecki
National Centre for Nuclear Research, Warsaw, Poland

M. Kuze
Tokyo Institute of Technology, Department of Physics, Tokyo, Japan

L. Ludovici
INFN Sezione di Roma and Università di Roma "La Sapienza", Roma, Italy

G. Nieradka and M. Suchenek
Nicolaus Copernicus Astronomical Centre, Polish Academy of Sciences, Warsaw, Poland

M. Ostrowski, L. Stawarz, and K. Zietara
Jagiellonian University, Astronomical Observatory, Cracow, Poland

M. Posiadala-Zezula
University of Warsaw, Faculty of Physics, Warsaw, Poland

P.J. Rajda and K. Stopa
AGH University of Science and Technology, Faculty of Computer Science, Electronics and Telecommunications, Cracow, Poland

C. Rott
Sungkyunkwan University, Department of Physics, Suwon, Korea

S.H. Seo
Center for Underground Physics, Institute for Basic Science, Daejeon, Korea

* also at TRIUMF

CONTENTS

I. EXECUTIVE SUMMARY

Water Cherenkov and water-based particle detector technologies are used to realize multi-kiloton scale experiments such as the currently operating Super-Kamiokande (Super-K) and T2K experiments, the planned Hyper-Kamiokande (Hyper-K) experiment and the proposed THEIA detector and ESSnuSB detectors. These experiments are operated or proposed to study a broad range of physics including neutrino oscillations, nucleon decay, dark matter and neutrinoless double beta decay. The Super-K and T2K experiments are entering new phases of measurements, with the loading of $Gd_2(SO_4)_3$ in Super-K for enhanced neutron detection, and the inclusion of new event topologies with final state pions in T2K. Understanding the new information from the inclusion of neutron and pion reconstruction will require dedicated measurements of how these hadrons are produced and propagate in water Cherenkov detectors. The neutrino oscillation programs of Hyper-K and ESSnuSB will also include kiloton scale near or intermediate detectors used to study neutrino production and interactions in the absence of neutrino oscillations, such as the Hyper-K Intermediate Water Cherenkov Detector (IWCD). Realization of these physics programs will require new detector technologies and percent level calibration of detector response and models of physics processes within the detector. Here we propose a 50 ton scale Water Cherenkov test experiment (WCTE) to be deployed in an East Area test beam line. The experiment will include a secondary target located just upstream of the experiment in order to produce very low energy particle fluxes, including charged pions. The WCTE measurement program will include a phase with loading of $Gd_2(SO_4)_3$ at a concentration of 0.2% by mass. The WCTE program will be carried out with the following objectives:

- Operate and understand the performance of new detector technologies such as multi-PMTs, and in a possible future phase, dichroicon wavelength-separating cones and water-based liquid scintillator in a fully integrated detector.
- Study the performance of a < 1 kiloton scale water Cherenkov detector with known particle fluxes, and test and develop calibration systems necessary for accurate modeling of a detector of this size.
- Measure important physics processes for the modeling of water Cherenkov detector response, including high-angle Cherenkov light production, pion scattering and absorption, and secondary neutron production in hadron scattering.

We aim to start operation of the water Cherenkov test experiment in 2023.

II. INTRODUCTION & MOTIVATION

Water Cherenkov detectors have long been used in experiments measuring or searching for low rate processes such as neutrino interactions or proton decay. A significant appeal of the technology is the capability to scale it to large detector masses of multiple kilotons. The currently operating Super-Kamiokande (Super-K) detector and proposed detectors such as Hyper-Kamiokande (Hyper-K), THEIA and the ESSnuSB detector will advance the water Cherenkov technology by adding new detection capabilities and by entering a regime of precision measurements not previously explored for GeV scale neutrino events.

The Super-K collaboration will soon load $Gd_2(SO_4)_3$ into the Super-K detector for enhanced neutron detection capability with captures on Gd. The neutron detection capability will expand the physics program with the ability to tag inverse β decay events, antineutrino interactions and atmospheric neutrino backgrounds for proton decay searches.

Hyper-K will make neutrino oscillation measurements with unprecedented precision, requiring systematic uncertainty at the 1% level or less. For this purpose, a new 1 kiloton scale Intermediate Water Cherenkov Detector (IWCD) is proposed to make precision neutrino rate measurements. The IWCD will utilize new high resolution photosensors in order to achieve the necessary performance for GeV scale neutrino interactions in a detector of less than 10 m in diameter. The Hyper-K experiment plans to use neutron tagging in measurements such as the supernova relic neutrino search or nucleon decay searches. Hyper-K, will be sensitive to uncertainties on neutron production in a manner similar to Super-K.

The THEIA experiment will deploy water-based liquid scintillator (WbLS) to increase the light output compared to a typical water Cherenkov detector and to add sensitivity to charged particles below the Cherenkov threshold. In order to detect and separate the directional Cherenkov light and isotropic scintillation light, new photosensor technologies are being developed that take advantage of the differing time and spectral distributions of Cherenkov and scintillation light.

The advancements in detection technology for water Cherenkov detectors listed above require extensive R&D programs that should include deployment of the prototype technologies in a test beam experiment with known particle energies and types entering the detector. Here, we propose a water Cherenkov test experiment (WCTE) in the CERN East Area beam line T9. The schematic overview of the WCTE can be seen in Fig 1. Tertiary particles are produced in a target located 8 m upstream of the water Cherenkov detector. A spectrometer consisting of a permanent magnet and tracking layers measures the momentum of tertiary particles. Particle identification for protons, pions and kaons is done with a time-of-flight (TOF) detector. Electrons are identified with an aerogel Cherenkov threshold detector. The water Cherenkov detector is instrumented with 128 multi-PMT photon detectors. Additional details of the motivation for the WCTE and details of the WCTE itself are provided in the following sections.

A. Hyper-Kamiokande Experiment and IWCD

Hyper-Kamiokande (Hyper-K) is a next-generation particle physics experiment with a broad physics program including neutrino oscillation measurements, nucleon decay searches, supernova burst and relic neutrino detection, and dark matter searches [1]. The Hyper-K detector, a 260 kiloton water Cherenkov detector, was approved by the Japanese government in January 2020. For the long baseline neutrino oscillation program, the Hyper-K detector will be used to study the oscillations of neutrinos produced at the J-PARC accelerator in Tokai, Japan. The core of the neutrino oscillation measurement program is the search for CP violation in the oscillation channels $\nu_\mu \rightarrow \nu_e$ and $\bar{\nu}_\mu \rightarrow \bar{\nu}_e$. Hyper-K will collect approximately 2000 candidate events in each of these oscillation modes after 10 years of operation, allowing for a measurement of the CP asymmetry with 3% statistical uncertainty. To take full advantage of the statistical power of the experiment, individual sources of systematic uncertainty must be controlled to the 1% level or better. Dominant sources of systematic uncertainty arise in the modeling of neutrino production, neutrino interactions and the detector responses.

Guidance on the necessary systematic error reduction for the Hyper-K CP violation measurement can be taken from evaluated systematic uncertainties for the similar measurement by the T2K experiment. Table I shows the systematic errors from T2K on the relative rate of electron neutrino and electron antineutrino candidates, the candidate events used for the CP violation search [2]. The total systematic error of 5.9% must be reduced for Hyper-K. Dominant systematic errors arise from the uncertainty on the modeling of the nuclear binding energy, 3.7%, and the uncertainty on the modeling of the cross section ratio for electron neutrinos and electron antineutrinos. To constrain the nuclear binding energy systematic, it is necessary to have near/intermediate neutrino detectors with energy scale known to 1% or better. The $\sigma(\nu_e)/\sigma(\bar{\nu}_e)$ cross section ratio uncertainty is a purely theoretical uncertainty, and may become even larger if uncertainties on nuclear effects are accounted for. A measurement of this cross section ratio requires using the $\sim 0.5\%$ of the beam that are ν_e or $\bar{\nu}_e$ from muon and kaon decays. Uncertainties on the modeling of the pion reinteractions in the Super-K detector or target nucleus are also important and may be improved with near/intermediate detector measurements of neutrino events with and without pions in the final state.

To reduce systematic uncertainties due to neutrino production and interaction modeling, the Hyper-K collaboration has proposed a suite of near detectors to study the neutrinos at short baselines before the oscillation effect is significant. This suite includes the Intermediate Water Cherenkov Detector (IWCD), based on the design of the previously proposed NuPRISM detector [3]. The IWCD, illustrated in Fig. 2, is a 10 m diameter by 8 m tall water Cherenkov detector deployed in a 50 m deep shaft about 1 km from the J-PARC neutrino source. The detector's elevation can be varied by

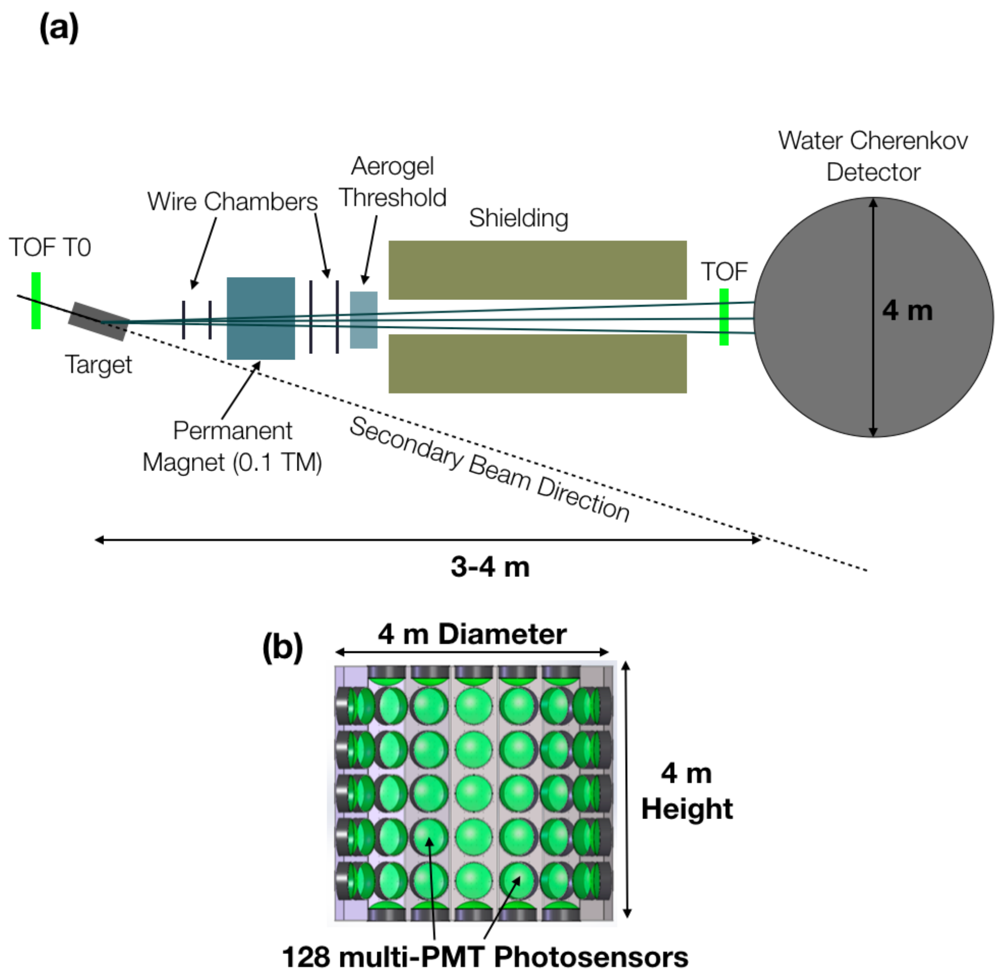

FIG. 1. (a) Top-down schematic overview of the WCTE in the secondary beam (not to scale). (b) Side-view cross section of the water Cherenkov detector shows the arrangement of the multi-PMT photon detectors.

TABLE I. Sources of systematic uncertainty on the measurement of CP asymmetry in T2K experiment [2]

Systematic Error Source	Uncertainty on $\nu_e/\bar{\nu}_e$ Candidates (%)
Super-K Detector Model	1.47
Pion Reinteractions	1.58
Near Detector Constrained Parameters	2.31
Nuclear Binding Energy	3.74
$\sigma(\nu_e)/\sigma(\bar{\nu}_e)$	3.03
NC1γ Production	1.49
Other NC Interactions	0.18
Total	5.87

controlling the water level in the shaft, allowing measurements to be made at varying angles relative to the average neutrino direction, probing different neutrino energies. The detector includes a 1 m thick optically separated veto region at the outer edge of the detector volume, leaving an 8 m diameter by 6 m tall region for physics measurements. The IWCD will be instrumented with newly developed multi-photomultipier tube (mPMT) photosensors with improved timing and spatial resolution to enable the event reconstruction performance necessary for a detector of this size.

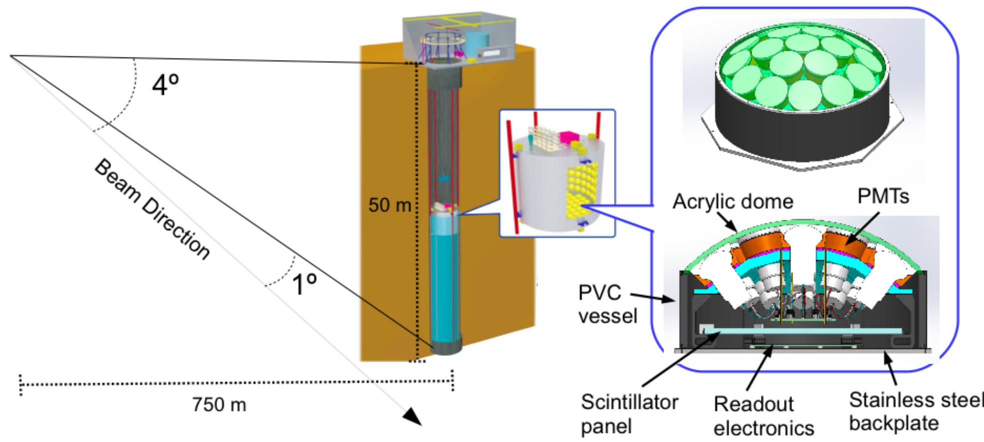

FIG. 2. Schematic overview of the IWCD.

The IWCD physics program will include three important measurements described here. Since Hyper-K will search for CP violation in the channels $\nu_\mu \to \nu_e$ and $\bar{\nu}_\mu \to \bar{\nu}_e$, it is necessary to measure the interaction cross section ratios $\sigma(\nu_e)/\sigma(\nu_\mu)$ and $\sigma(\bar{\nu}_e)/\sigma(\bar{\nu}_\mu)$ with precision of 3-4% or better. This measurement requires controlling relative uncertainties on the modeling of the detector response to $\nu_e(\bar{\nu}_e)$ and $\nu_\mu(\bar{\nu}_\mu)$ at the 2% level or better. This requires precise understanding of the event reconstruction efficiency, particle identification efficiency and vertex reconstruction, which affects the effective fiducial mass, in the candidate interactions. The particle identification in particular is important for this measurement. Since the beam only consists of $\sim 0.5\%$ ν_e or $\bar{\nu}_e$, the backgrounds from muons and pions must be reduced 2-3 orders of magnitude to achieve a pure sample of electron (anti)neutrino candidates. The capability of the WCTE to study particle identification will be discussed later.

The IWCD will also study the energy dependence of neutrino interactions by making measurements with the detector located at different off-axis angles, allowing the neutrino spectrum to vary. These measurements require that the detector response be maintained within 1% during operation to ensure unbiased interpretation of the off-axis angle dependence of the measurements. The measurements at different off-axis angles will be used to relate the reconstructed final state topologies and kinematic properties to the neutrino energy. Hence, correct modeling of the efficiency to detect final state particles and reconstruct their kinematic properties will be critical. This includes the reconstruction of final state pions, which may undergo hadronic interactions in the detector. The interpretation of the measurements at varying off-axis angles requires an energy scale uncertainty of 0.5% or less for the IWCD. The vertex reconstruction must also be biased by less than 1 cm to control the uncertainty on the fiducial mass. Understanding the reconstruction of pions and evaluating calibration methods to control energy scale and vertex bias errors are goals of the WCTE.

The IWCD will also be used to measure with high statistics the production of neutrons in neutrino interactions. This will be achieved by loading the detector with $Gd_2(SO_4)_3$ to enhance the neutron capture cross section and increase the efficiency to reconstruct neutron capture events. These measurements will be used as inputs to Super-K and Hyper-K neutrino and nucleon decay analyses that use neutron multiplicity measurements to identify signal or background events. The interpretation of the IWCD neutron multiplicity data will require an understanding of the secondary neutrons produced when various final state particles traverse the detector medium. This secondary neutron production can be measured in the WCTE.

To achieve the full physics sensitivity of Hyper-K and IWCD, it is necessary to calibrate the detectors and understand the detectors' responses with about 1% accuracy. This includes unbiased modeling of the energy scale, detection efficiency, particle identification and the fiducial region in the event simulation and reconstruction. The WCTE will provide a platform to develop the percent level calibration techniques with particle fluxes of known type and kinematic properties. The WCTE will also probe important physics processes for the understanding of final state signatures, such as the production of high energy delta rays that produce Cherenkov light, the scattering and absorption of pions in the detector, and the secondary production of neutrons in the detector.

The Hyper-K and IWCD detectors will use a number of unique detection and calibration techniques, such as the multi-PMT photosensor, discussed in Section III B, and the photogrammetry position calibration discussed in Section III F. The multi-PMT photosensor has been chosen as the photosensor for use in the IWCD, while it is considered as a supplementary photon detection system to the 20-inch diameter PMTs that will be installed in Hyper-K. The application of the photogrammetry calibration is new for the water Cherenkov detector program in Japan. These new systems and other should be evaluated in a full-scale detector before installation in IWCD and Hyper-K to ensure that they will meet the necessary performance requirements. The WCTE is the ideal location to evaluate the performance of these systems.

B. Super-Kamiokande and T2K

The Super-Kamiokande (Super-K) detector is a 50 kilo-ton water Cherenkov detector that has operated since 1996 [4]. The broad physics program of Super-K includes atmospheric and solar neutrino oscillation measurements, nucleon decay searches, supernova neutrino detection and dark matter searches. The Super-K detector also acts as the far detector for the T2K long baseline neutrino oscillation experiment. In T2K, a beam of neutrinos or antineutrinos is produced at the J-PARC facility on the east coast of Japan and the neutrino oscillation effect is detected in Super-K, after the neutrinos travel 295 km [5]. Super-K and T2K have produced a number of groundbreaking measurements in the field of neutrino oscillations, including the discovery atmospheric neutrino oscillations by Super-K [6], and the discovery of muon neutrino to electron neutrino oscillations by T2K [7]. Both Super-K and T2K plan to operate until the start of Hyper-K, and will implement new experimental configurations and analysis techniques in the coming years.

The Super-K collaboration is now in the process of loading up to 0.2% $Gd_2(SO_4)_3$ into the Super-K detector to enhance the capability to detect neutrons [8, 9]. With the 0.2% loading fraction, approximately 90% of neutrons produced in Super-K will capture on Gd nuclei, which then deexcite with the production of high energy gamma rays that can be detected with high efficiency. The reconstruction of neutrons will help a number of analyses carried out by the T2K and Super-K collaborations. As shown in Fig. 3 in the quasi-elastic scattering mode, a neutrino will typically produce a proton in the final state, while an antineutrino will produce a neutron. The absence of a neutron can be used to tag an event as neutrino-like. However, as illustrated in Fig. 3(c), a neutron may be produced in a neutrino event through the secondary interaction of the proton with oxygen nuclei in the detector. These secondary interactions and final state interactions of the proton in the target nucleus decrease the fraction of neutrino quasi-elastic scattering interactions with no neutrons from 100% to $\sim 60\%$ according to the Super-K simulation, as shown in Fig. 4. Fig. 4 also shows that quasi-elastic interactions, the main signal mode for many analyses in T2K and Super-K, will tend to have more neutrino interactions with no neutrons compared to non-quasi-elastic interactions. This suggests that neutron tagging information can also be used to statistically separated quasi-elastic and non-quasi-elastic interactions.

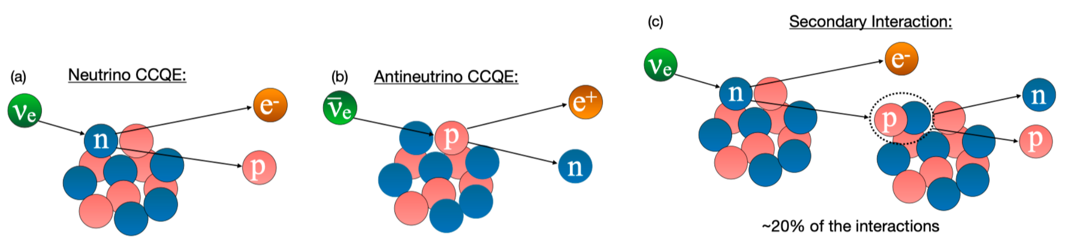

FIG. 3. Schematics of neutrino and antineutrino quasi-elastic scattering on nuclei are shown in (a) and (b). The process of secondary interactions that can produce a neutron in a neutrino event is shown in (c).

The secondary production of neutrons by protons or pions produced in neutrino interactions is not yet well constrained by data. With loading of $Gd_2(SO_4)_3$ in the WCTE, it will be possible to measure the secondary neutron production in the WCTE. Fig. 5 shows the proton spectrum for neutrino interactions in T2K and the expected proton spectrum for the tertiary production configuration for the WCTE as described in Section III A. The WCTE will accumulate proton fluxes ranging from 0.3 GeV/c to >1.2 GeV/c with sufficient statistics to make precise measurements of secondary neutron production. This covers most of the range relevant for T2K and Super-K.

The T2K experiment plans to further expand the sensitivity of neutrino oscillation measurements by included samples where one or more pions are detected in the final state of the (anti)neutrino interactions [11]. In T2K and Super-K, the typical hadronics scattering length of pions is similar to their travel distance through the detector, so pions often undergo hadronics scattering in the detector. These pion scatters affect the identification and kinematic reconstruction

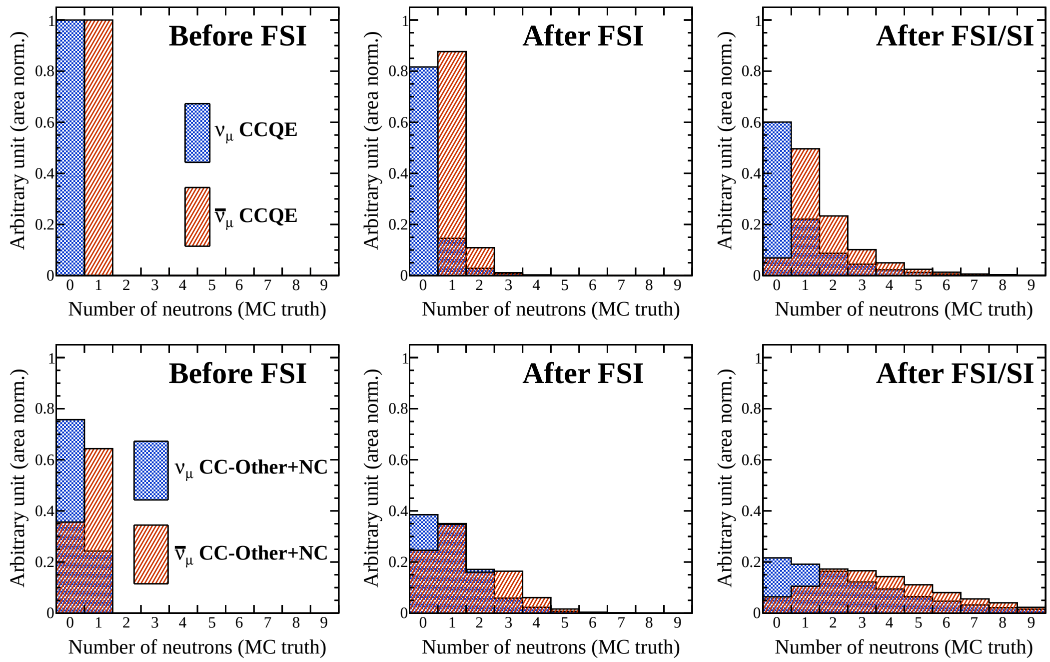

FIG. 4. The number of neutrons in neutrino-nucleus interactions in T2K after the initial neutrino-nucleon interaction (left), after the final state interactions inside the target nucleus (center), and after secondary interactions in the detector (right). The top plots show charged current quasi-elastic interactions, while the bottom plots show non-quasi-elastic interactions.

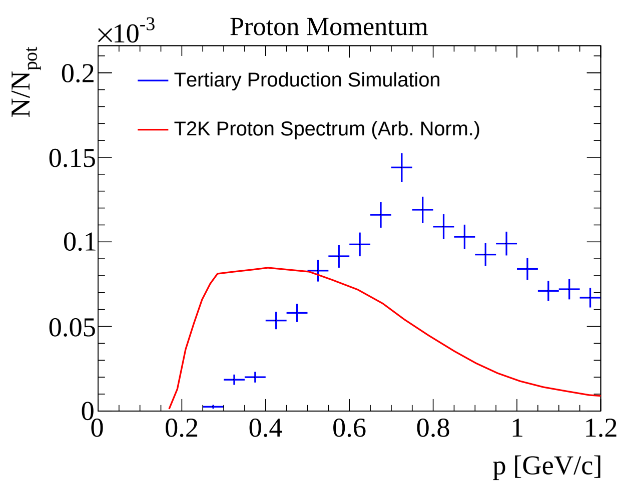

FIG. 5. The proton spectrum for neutrino interactions in T2K near detector (digitized from [10]) and the WCTE.

of effects, and mismodeling of the scattering can introduce systematic biases in the analysis. The scattering is modeled by the NEUT cascade model, which is tuned to pion scattering data [12]. Fig. 6 shows the fit of the NEUT cascade model to oxygen data that is relevant for the modeling of pion propagation in Super-K. From the figure, one can see that π^{+}+O data is sparse. In fact the fit relies on the model to extrapolate constraints from other targets, such as π^{+}+C, where more data is available. This introduces strong model dependence into analyses that use pion information, and may deter T2K and Super-K from using the kinematic information of pions in analyses.

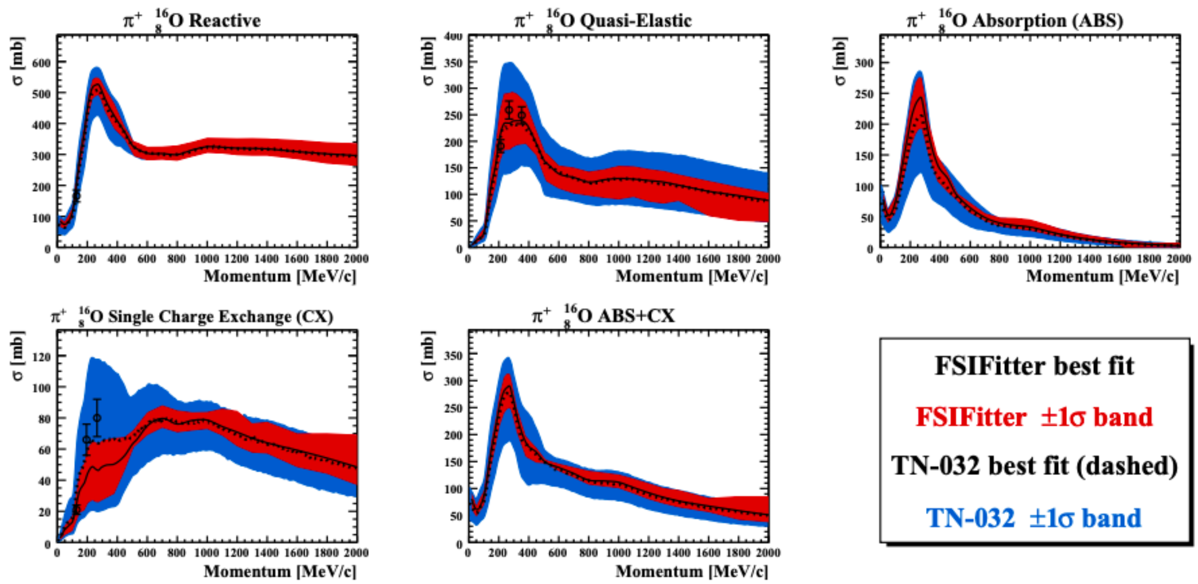

FIG. 6. Fit of the NEUT cascade model to π^{+}+O data from [12]. The plots are for the total reactive cross section (upper left), the quasi-elastic cross section (upper center), the absorption cross section (upper right), the charge exchange cross section (lower left), and the absorption+charge exchange cross section (lower middle). The dashed and solid black lines show the central value of the model fit for two different versions of the fitting framework, and the red and blue error bands are from each of those fits, respectively.

In the WCTE experiment, we will not measure π^{+}+O scattering cross sections since the experiment is not in a configuration where the target material is a small fraction of the hadronic scattering length, which is typical of interaction cross section experiments. Rather, with the WCTE it will be possible measure the full water Cherenkov detector response for pions as they propagate through the detector and undergo any number of hadron scattering processes. Fig. 7 shows a schematic example of a π^{+} event that includes both quasi-elastic and charge exchange processes. Such an event can have up to four distinct Cherenkov rings from the pion interaction chain. In the WCTE, it will be possible to collect data that maps between the incoming pion momentum and the observed final states, including the number of rings, their energies and their directions. This data will be valuable for validating and tuning simulations in T2K and Super-K.

C. THEIA Detector

The proposed Theia detector would deploy Water-based Liquid Scintillator (WbLS) to allow for the simultaneous detection of both Cherenkov and scintillation light. The physics program for such a detector is broad, ranging from solar neutrino measurements and an eventual search for neutrinoless double beta decay to long-baseline neutrino physics in the LBNF beamline and the search for nucleon decay. At low energies, the scintillation signal provides additional light collection to improve the energy resolution and identify most of the radioactive backgrounds, whereas the Cherenkov light provides direction reconstruction to improve background discrimination. At higher energies, WbLS can provide additional discrimination between various multi-particle final states by providing extra sensitivity to particles not typically seen in a traditional water-Cherenkov detector, such as low energy protons.

These potential benefits can only be realized if the additional scintillation light does not substantially degrade the reconstruction performance relative to a pure Cherenkov detector. Several experiments, such as ANNIE and WATCHMAN, are planned to study the performance of WbLS from a neutrino source, but event reconstruction outputs, such as particle identification, depend on exploiting subtle differences in the detected light patterns, and such effects are difficult to study in neutrino interactions due to uncertainties in the kinematics of final state particles from these interactions. The

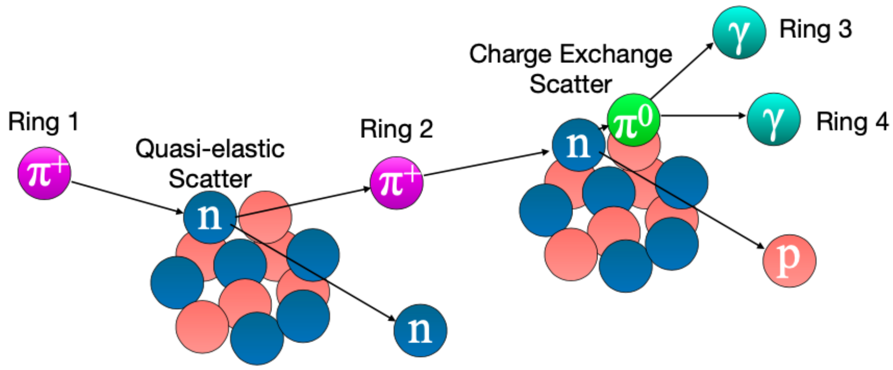

FIG. 7. Example of pion scattering processes that can take place in the WCTE. In this case, the pion first undergoes a quasi-elastic scatter and then charge exchange. In total, up to four distinct Cherenkov rings can be produced.

development of WbLS and dedicated photon detectors for WbLS-based detectors is not yet at the stage to propose a concrete measurement program in the WCTE. At this stage, we discuss the potential to deploy WbLS and associated photon detectors in the WCTE apparatus in Appendix A, but we don't propose a WbLS phase of operation at this time.

D. ESSnuSB Experiment

The ESSnuSB experiment [13, 14] proposes to use a neutrino super beam generated at the European Spallation Source (ESS) with a beam power of 5 MW and primary proton energy of 2.5 GeV. The spectrum of neutrinos produced at the ESS will have a mean energy of 0.4 GeV. At a baseline of 540 km, the neutrino spectrum is peaked at the second oscillation maximum, allowing for an enhanced measurement of the CP violation effect compared to measurements at the first oscillation maximum. A megaton scale water Cherenkov detector with a fiducial mass of 500 kilotons, based on the design of the MEMPHYS water Cherenkov detector elaborated in the earlier EU Design Studies, and shown in Fig. 8, is proposed. This detector will take advantage of improvements to photon detector performance in a similar manner as the Hyper-K detector, and will be sensitive to many of the same systematic uncertainties. The ESSnuSB experiment will also require a near detector to control systematic uncertainties on the modeling of the neutrino production and neutrino interactions. Currently the performance of a small water Cherenkov counter as part of this Near Detector is being investigated through simulations. A kiloton scale intermediate detector with the varying off-axis capability similar to the IWCD is another near detector option that may be considered. The ESSnuSB project will benefit from the WCTE as it will provide a platform to study and develop the detection technologies that are being considered for the ESSnuSB experiment.

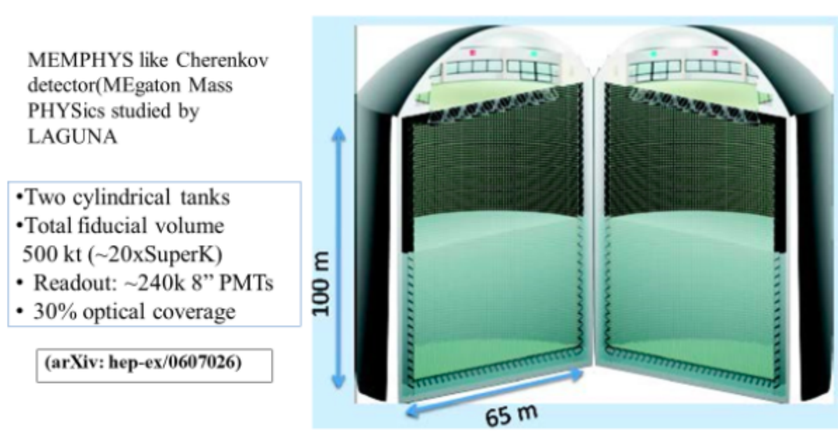

FIG. 8. Drawing of the MEMPHYS water Cherenkov detector design.

E. Water Cherenkov Test Experiment Overview

The conceptual drawing of the WCTE is shown Fig. 1. The water tank for the detector has a diameter of 4.1 m and a height of 4 m. The goal of the experiment is to measure the properties of charged particles of type $\pi^{\pm}$, p^{+}, $e^{\pm}$, $\mu^{\pm}$ and $K^{\pm}$ with incident momenta ranging from ~ 200 MeV/c to ~ 1200 MeV/c as they traverse the detector. The configuration with tertiary particle production < 5 m upstream of the detector is necessary to achieve the low momentum pion fluxes. The secondary target is placed close to the detector so that low momentum pions can reach the detector before decaying. This configuration requires careful design of the shielding and orientation of the spectrometer and detector so that background tertiary particles are minimized. For incident $\mu^{\pm}$, the T9 beam line will be run in the lowest momentum configuration, and muons will taken directly from the beam line.

The WCTE will have two phases of operation. The first phase will use standard ultra-pure water and the deployment of multi-PMT photosensors and calibration systems that will be used in the IWCD. The goal of this phase is to match as closely as possible to the detector configuration that will be used in the initial phase of the IWCD. Fig. 9 shows the arrangement of the multi-PMT photosensors in the detector. For full instrumentation, 128 multi-PMT modules will be installed and operated. The WCTE will allow the performance and calibration of the detector and its components to be evaluated.

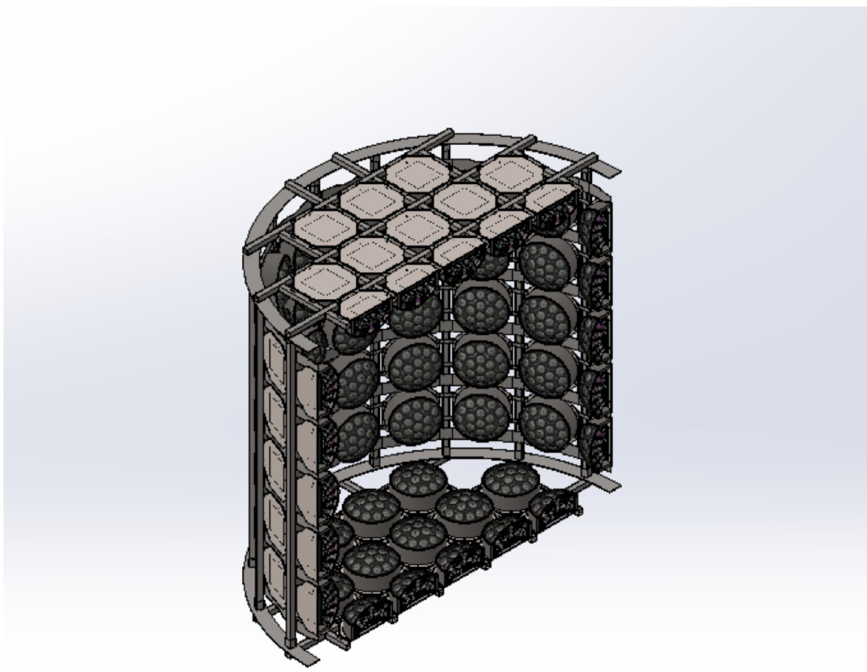

FIG. 9. Cross section drawing of the multi-PMT layout inside the detector.

Fig. 10 shows example reconstructed vertex and momentum distributions for simulated 300 MeV electron events in the WCTE for particles entering at the center of the upstream side of the tank, as well as particles produced at the center of the IWCD tank. The resolution for reconstructing the vertex, momentum and particle type in the WCTE is similar to the IWCD, indicating that the WCTE is a useful platform to evaluate the performance of detection and calibration systems to be used in the IWCD.

Fig. 11 shows example distributions of the reconstructed particle identification (PID) variables for 400 MeV/c electrons, muons and pions. To achieve pure samples of electron (anti)neutrino candidates on the IWCD, it is necessary to reduce the muon background by more than three orders of magnitude. The pion background must also be significantly reduced to remove neutral current events with the production of single pions. This reduction is achieved with cuts on the PID variable shown in Fig. 11 and a cut on the presence of a Michel electron. The remaining muon that "fake" an electron populate the tail of the muon PID distribution. It is important to study these events with a well controlled sample of muons to ensure that the properties which cause them to populate the tail of the distribution are well modeled by the simulation. The pions tend to populate the space between the true muon and electron distributions due to the hadronic scattering of the pions. Modeling the pions that "fake" an electron will depend on an accurate model of hadronic scattering in the detector. The physics models of muons and pions in the simulation will be tuned and verified by the WCTE data, which will include samples of pions and muons of known energy and direction.

The initial phase of the WCTE will also be used to evaluate important physics processes that are necessary for the accurate modeling of the detector. For example, the production of Cherenkov light at large angles relative to the particle propagation due to delta rays will be measured. The timing resolution of the multi-PMT photosensors, $\sim$ 700 ps RMS, corresponds to a travel distance of 15 cm in the detector, allowing high angle light from delta rays or scattering to be separated from light produced by reflections. The initial phase will also be used to study the properties of pion scattering in the detector, which can produce topologies with more than one Cherenkov ring for each initial charged pion, or rings that are not completely filled in if the pion is absorbed before dropping below the Cherenkov threshold.

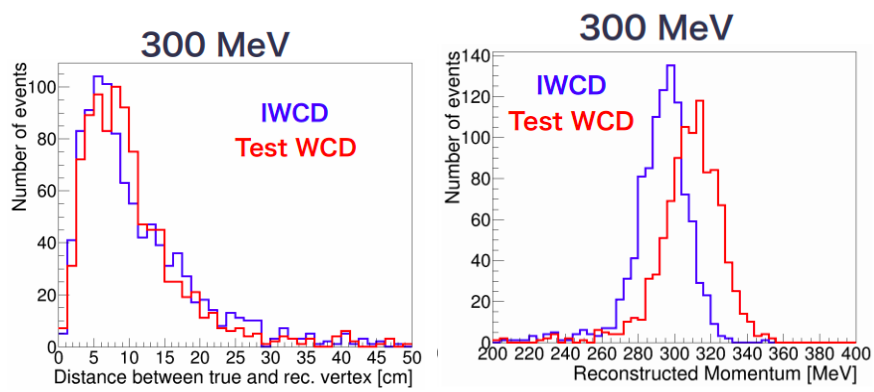

FIG. 10. Vertex resolution (left) and momentum resolution (right) for reconstructed 300 MeV/c electrons simulated in the the WCTE (red) and IWCD (blue). The bias in the WCTE momentum resolution is due to incomplete tuning of the reconstruction code for the smaller detector geometry.

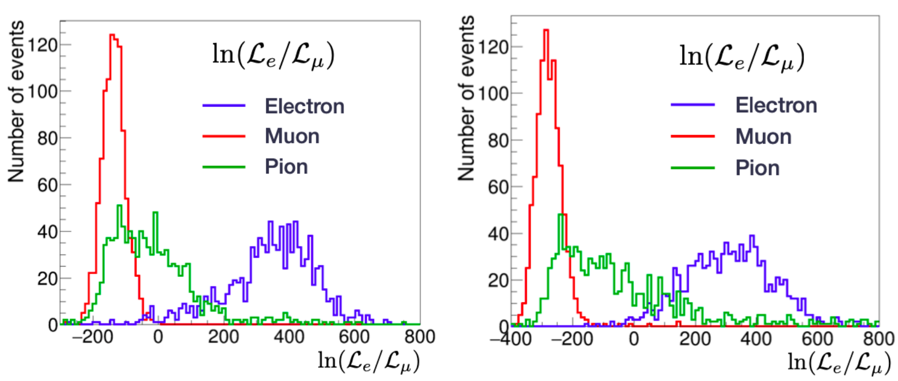

FIG. 11. Distributions of true 400 MeV/c e^-, μ^- of π^- particles plotted in the particle identification variable, the log-likelihood ratio for electron and muon hypotheses, for the WCTE (left) and IWCD (right).

The angular distribution of Cherenkov photons emitted by charged particles is a critical input to water Cherenkov detectors. Small changes to the shape of this distribution can bias both the reconstructed momentum, and the position of the reconstructed particle vertex along the direction of particle movement. The WCTE will make precise measurements of the Cherenkov angle distributions for electrons, muons, pions, and protons over the range of beam momenta most relevant to current and future water Cherenkov experiments.

To assess the potential variations in the modeling of the Cherenkov production, a simulation was produced to compare the model used for the Super-Kamiokande detector, the GEANT3-based SKDETSIM, with the model used in simulations of the Hyper-Kamiokande detector, the GEANT4-based WCSim. To make this comparison, muons were simulated in

SKDETSIM, and the initial position, direction, wavelength, and polarization of each Cherenkov photon was recorded. These photons were then fed into a WCSim simulation of both the Super-Kamiokande detector, and the WCTE detector. The output hit and charge distributions on each of the PMTs were then compared to the distributions produced by muons directly simulated within WCSim.

The results of these comparisons between SKDETSIM and WCSim for 50,000 muons generated with 300 MeV/c are shown in Figure 12. The top-left plot shows the true angular distribution of Cherenkov photons immediately after they are produced. There is a clear discrepancy in the outer edge of the Cherenkov ring between the 2 models, and the amount of light in the backward direction is much higher in SKDETSIM relative to WCSim. The top-right plot shows the reconstructed charge distribution in the Super-Kamiokande detector. The differences in the true Cherenkov distribution are clearly detectable, and this level of discrepancy has been shown to produce shifts in the reconstructed vertex position outside of the nominal vertex resolution. The bottom plot shows the same comparison within the WCTE detector. The same feature seen in the Super-Kamiokande detector can be seen within WCTE, although the effect is somewhat reduced due to the higher levels of reflected photons in the smaller-sized detector.

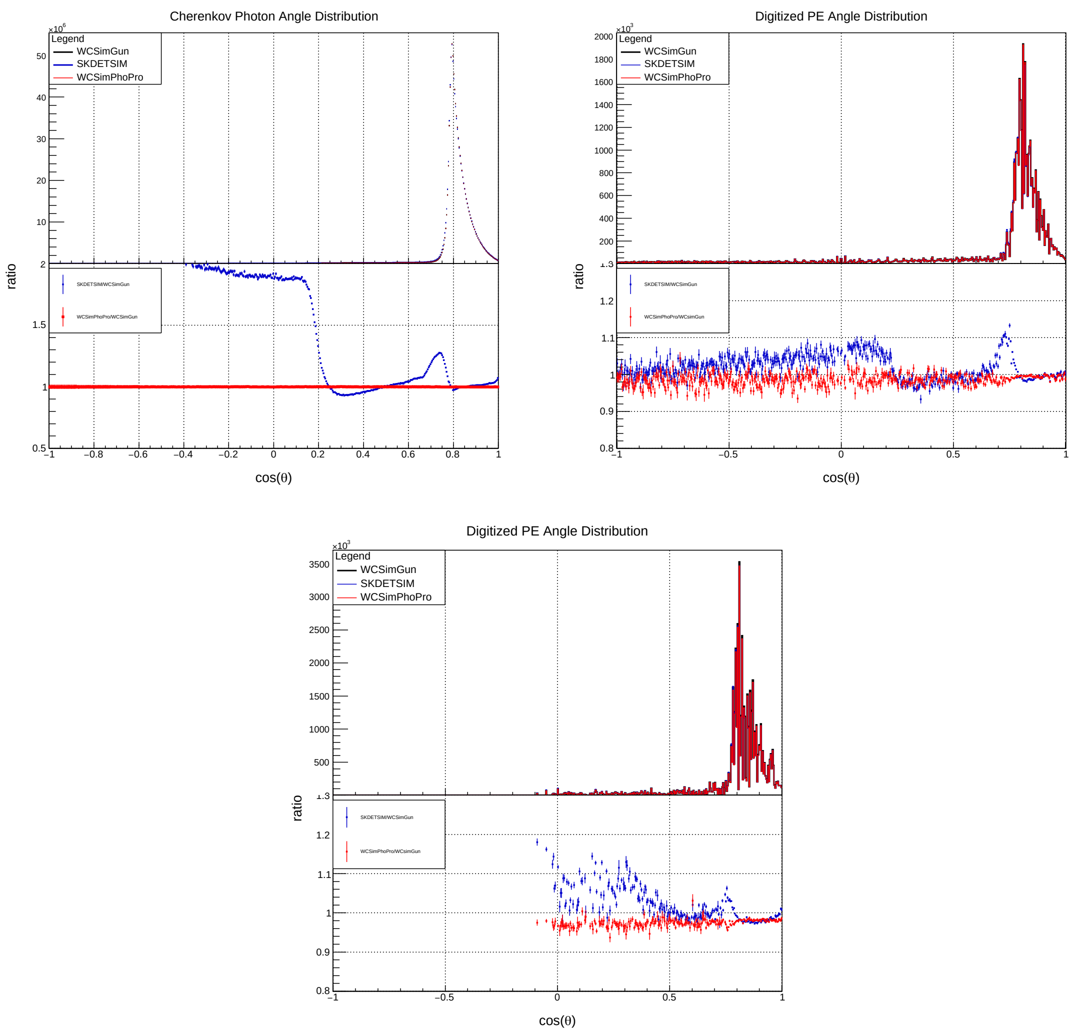

FIG. 12. The Cherenkov angular distribution is shown for true photon angles (top-left), reconstructed charge distributions in the Super-Kamiokande detector (top-right), and reconstructed charge distributions in the WCTE detector (bottom).

The WCTE will be sensitive to differences in the modeling of Cherenkov photons in GEANT3 and GEANT4, as well as additional GEANT4 models of particle propagation/scattering not shown here. This will provide valuable feedback for current and future water Cherenkov detectors.

The second phase of the experiment will include loading with $Gd_2(SO_4)_3$ to enhance the neutron detection capability of the detector. Super-K and Hyper-K will use measured neutron multiplicities in neutrino interactions to make statistical separation of neutrinos and antineutrinos or exclusive final states in neutrino interactions. Neutron detection will also be used to tag atmospheric neutrino interactions that are backgrounds to nucleon decay searches. To properly model the neutron production and detection, it is necessary to model the production of secondary neutrons as particles traverse and interact in the detector medium. During this phase, the production of neutrons from particles propagating through the detector will be measured.

Fig. 13 shows the predicted multiplicity of detected neutrons when a primary hadron traverses a generic water Cherenkov detector of sufficient size. Significant production of secondary neutrons is expected and the prediction varies depending on the model. The WCTE with $Gd_2(SO_4)_3$ loading will be able to measure these neutron multiplicities. In addition to the neutron production from hadrons, the neutron production from μ^- capture on O nuclei will be measured. This process is another source of secondary neutron production. These neutrons can provide another source of statistical separation of neutrinos and antineutrinos (μ^- and μ^+) in muon (anti)neutrino charge current interactions.

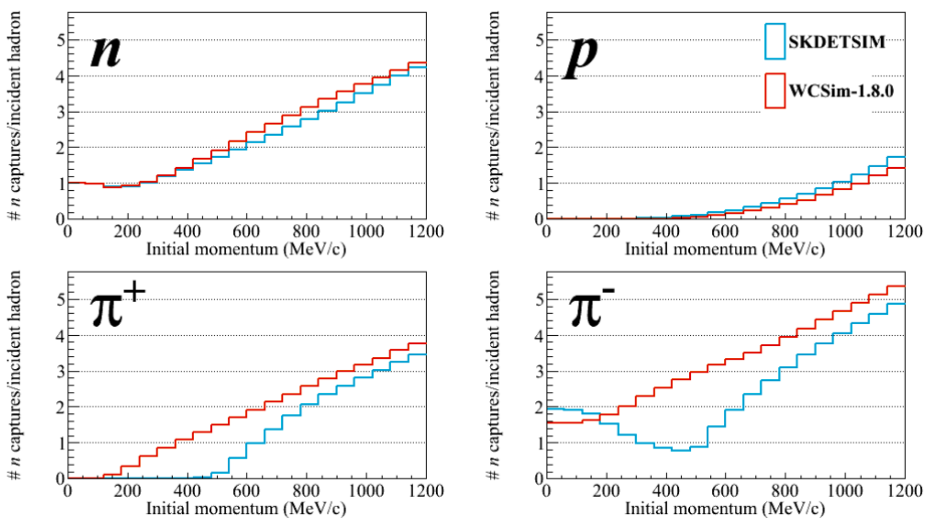

FIG. 13. Detected secondary neutron production multiplicities for neutrons produced by hadrons propagating in a water Cherenkov detector. Simulated with GEANT4-based WCSim and SKDETSIM, the simulation package for Super-K.

The capability of the WCTE to detect secondary neutron production is simulated using a flux of 500 MeV/c π^- entering the upstream end of the WCTE. Fig. 14 shows the true and reconstructed vertices of neutron capture events, where the true vertices include neutrons that leave the detector and interact in the surrounding air. 90% of the produced neutrons are captured inside the tank and 84% of those neutrons are detected if the fiducial region extends to the edge of the detector. The fiducial region may be restricted to reduce external backgrounds or backgrounds due to radioactivity in the mPMT material. In this case the efficiency to detect neutrons in the fiducial region is 63% or 48% if the vertex is required to be 25 cm or 50 cm from the detector wall respectively. Fig. 14 also shows the vertex position reconstruction resolution, which is 24 cm. From this simulation study, we can see the capability of the WCTE to effectively detect secondary neutron production.

The experimental apparatus established for the WCTE may be used for future test experiments that will deploy new technologies such as water-based liquid scintillator (WbLS) or novel photodetectors such as dichroicon photodetectors or large area picosecond photodetectors (LAPPDs). Discussion of potential future uses of the WCTE apparatus can be found in Appendix A.

III. EXPERIMENTAL APPARATUS

In this section, we provide a brief description of the components of the water Cherenkov test beam experiment, including the detector and beam components.

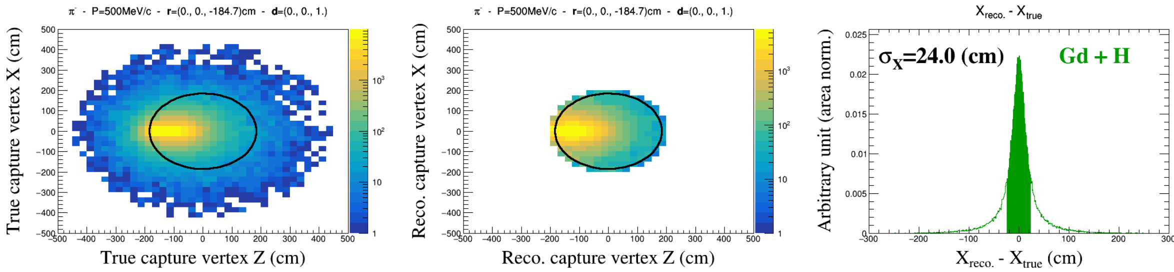

FIG. 14. Simulated neutrons from 500 MeV/c π^- entering the upstream side of the WCTE. Left: The true vertex of neutron captures, including captures outside of the tank in air. Middle: The reconstructed vertex of neutron captures in the detector. Right: The vertex resolution of reconstructed neutron capture events

A. Beam-line, Secondary Target and Spectrometer

As suggested in the previous subsection, the water Cherenkov detector will be placed in a charged particle beam which includes $e^{\pm}$, $\mu^{\pm}$, $\pi^{\pm}$, and p. The desired momenta are between 140 MeV/c and 1200 MeV/c. The requirement of low momentum pion and muon beams is placing a conflicting constraint on the WCTE. To get low momentum pions in the desired energy range, the beam-line must be less than 10 m long. On the other hand, muons are products of pion decays and to achieve low momentum muon beam, the beam-line should be longer to allow most of the pions to decay. Therefore, we need to run the WCTE in two different configurations: a short setup with pion enhanced beam and a long setup with muon enhanced beam.

The CERN East Area, the most suitable area for the WCTE, receives a 24 GeV/c primary proton beam from Proton Synchrotron (PS) and generates secondary hadron and electron beams from 0.3 GeV/c and 15 GeV/c. The secondary beam intensity is up to $5 \cdot 10^6$ particles per spill. While the secondary beam-line is too long to provide a low momentum pion beams, it can provide a low momentum muon beam.

The spectrometer setup

To generate low momentum hadron beams we propose a secondary target and a compact spectrometer placed several meters upstream from the water tank. A compact neodymium dipole magnet Fig. 15) together with silicon strip layers will be used for tracking and momentum measurement. Since the tertiary beam will include both, positive and negative particles, second neodymium magnet will be used to compensate the beam divergence caused by the first magnet. The magnet design is shown in Fig. 15, while the size of the tertiary beam spot on the tank surface is shown in Fig. 16. The secondary compensation magnet significantly reduces the beam size and removes the correlation between the x hit position on the tank wall and particle momentum and charge.

We have developed a Monte Carlo simulation based on GEANT4.10.05.p1 to study the spectrometer performance and to estimate the produced particle rate. All hadronic interactions are simulated with FTFP_BERT physics list. Simulated geometry includes two Halbach array magnets and eight silicon strip planes. The planes are placed in pairs to measure x and y particle positions. Two pairs are located upstream from the first magnet and the other two are downstream from the first magnet. To estimate the momentum resolution we assume a 60 μm pitch, silicon thickness of 300 μm, and 300 μm of carbon fiber support per plane. The distance between two pairs of planes on each side of the magnet was set to 20 cm. The expected momentum resolution has been studied by reconstructing track parameters of low momentum pions passing through the magnet and the tracking layers. The obtained resolution presented in Fig. 17 is satisfactory for the WCTE. However, the resolution can be easily improved if more precise detectors with reduced material budget are used or the separation between the wire chambers is increased.

Since the beam will be generated close to the water Cherenkov detector, a choice of the target, beam momenta, and the shielding configuration need to be taken into careful consideration to avoid high background particle rates. In this study, we have used a 2 cm long tungsten target and 12 GeV/c proton beam to simulate the typical secondary beam momenta in the East Area. The center of the water tank has been placed at 5.5 m from the target. The beam and the target are angled at 450 mrad with respect to the axis between the target, spectrometer and the water tank. The angle has been chosen so that surviving beam particles miss the magnets and the water Cherenkov detector. Concrete shielding has been placed around the iron collimator to block most of the produced particles which are not going through the spectrometer. The total thickness of the concrete shielding is around 350 cm. The simulation geometry is shown in Fig. 18.

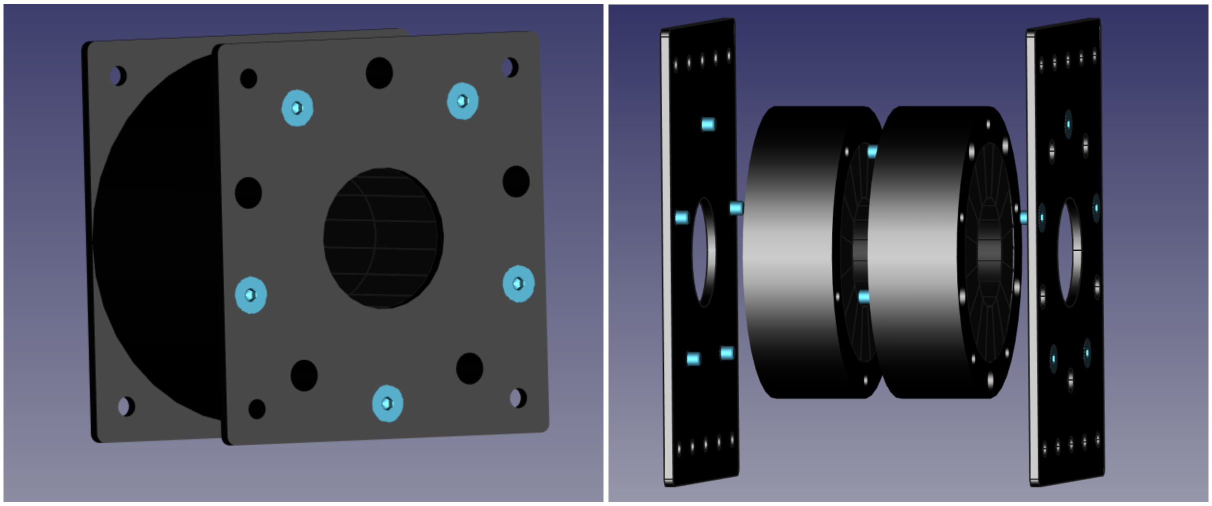

FIG. 15. A CAD design of the neodymium Halbach array magnet (left) and individual magnet components (right). The magnet consist of two dipole Halbach rings encased in the stainless steel cylinder and two square endplates. Each endplate includes M5 mounting holes that can be used for mounting the magnet to 40×40 cm^2 aluminium extrusions.

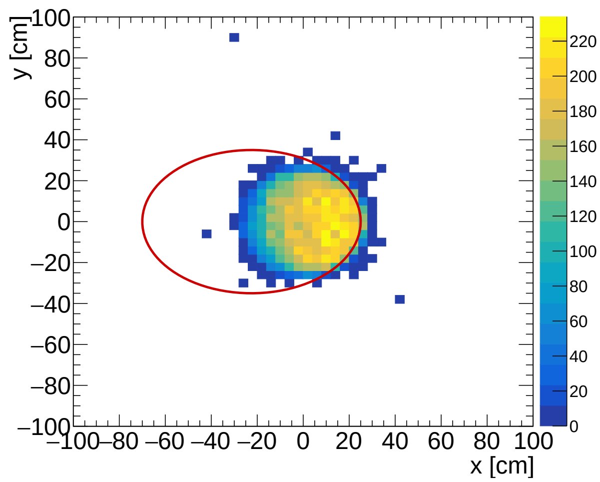

FIG. 16. Tertiary beam spot size on the tank surface. The red ellipse shows the beam spot size and position if the compensation magnet is not used.

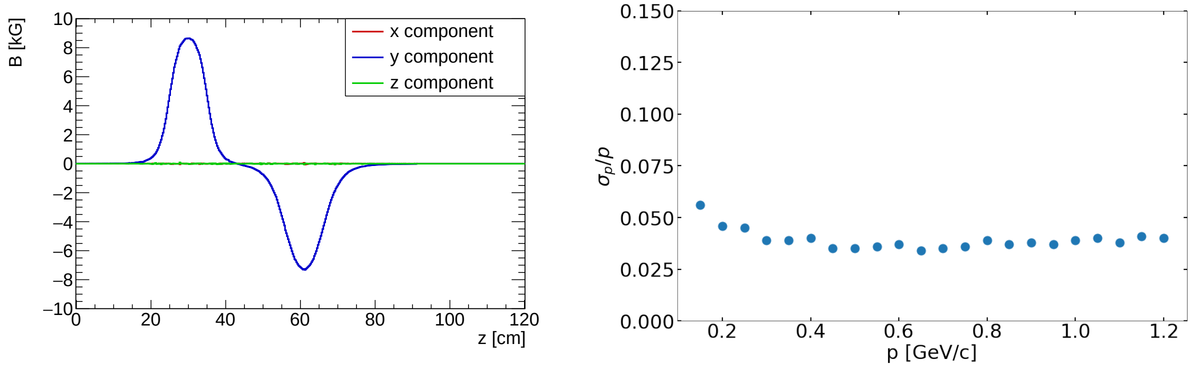

FIG. 17. The combined magnetic field of two Halbach arrays (left) and the momentum resolution calculated with the field of the first magnet.

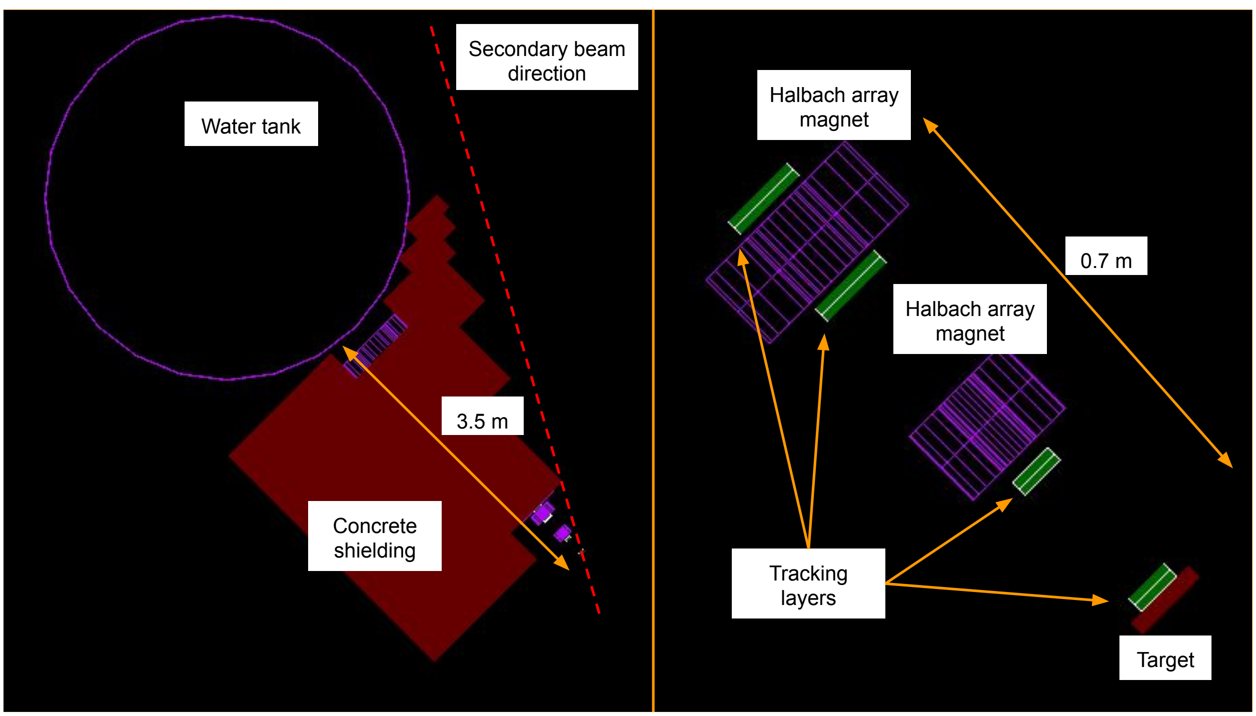

FIG. 18. The top view(left) and the downstream view (top right) of the Monte Carlo event display with a single surviving beam particle.The zoomed in view of the spectrometer is shown in the bottom right panel.

TABLE II. Integrated tertiary particle rates between 0.2 GeV/c and 1.2 GeV/c for for 10^6 secondary beam protons at 12 GeV/c.

e^-	e^+	π^+	π^-	p
143	181	1193	1053	1502

The results of the simulation for pion and proton beams are presented in Fig. 19. The particle rate is defined as a number of selected tertiary particles per incoming secondary beam particle. Tertiary particles are selected if they are within the acceptance of the magnet and the collimator with eight hits in the tracking layers. In addition, events with more than one selected tertiary particle are discarded, since that would create multiple rings in the water Chenerkov detector. The integrated rates in the momentum region between 0.2 GeV/c and 1.2 GeV/c are shown in Tab. II.

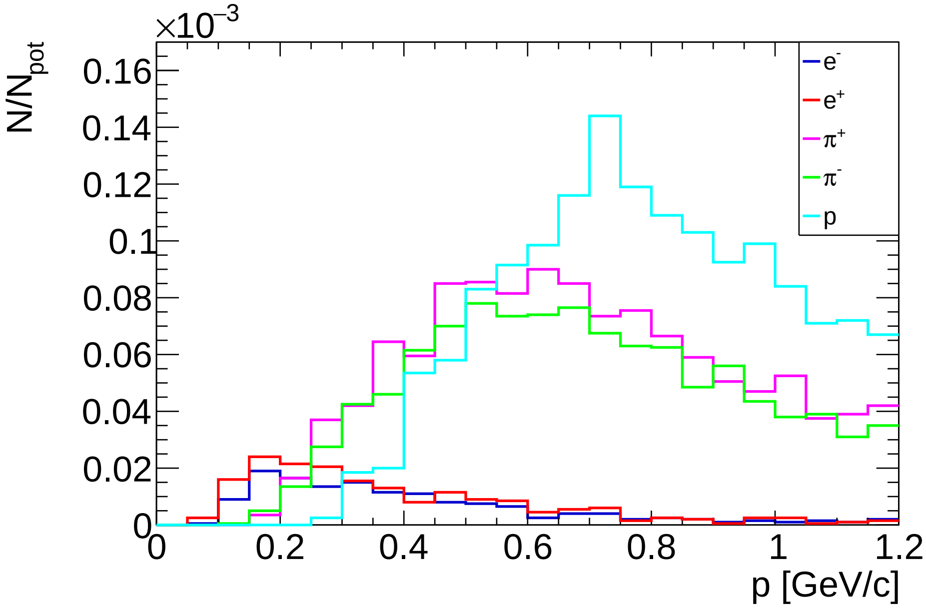

FIG. 19. The tertiary beam rate hitting the cross-section of the water tank.

The tertiary beam background

The background includes all particles entering the tank without eight hits in the tracking layers. The main sources of background are neutrons, gamma rays, and electrons created in the target, magnet and shielding. Additional background is created by pion decays inside the collimator.

The number of background particles arriving in coincidence with the selected particles is estimated in Fig. 20. Tertiary pions and protons are on average, accompanied by fewer than one background particle. Additionally, more than 50% tertiary protons and pions do not have any background particles hitting the tank in coincidence. On the other hand, tertiary electrons and positrons have significant γ ray background that can make measurements of electrons in the water Cherenkov detector difficult. However, cleaner sample of low momentum electrons and positrons can be obtained from the secondary beamline. Momentum distributions of the background particles is shown in Fig. 21. Around 90% of background electrons and γ rays accompanying tertiary beam pions and protons have momentum below 20 MeV/c. Therefore, they will be absorbed in the first several cm of water. By using the fiducial volume cut in the water Cherenkov detector it is possible to completely remove this background. Similarly, more than 80% of neutrons have momentum below 200 MeV/c and can be easily removed by the fiducial volume cut.

Muons from pion decays can create significant background if not identified properly. Segmented time-of-flight detector placed between the collimator and the water tank can be used to identify kinks in the tertiary beam trajectories. The channel width of 1 cm is good enough to remove $\sim 99\%$ of muon background (see Fig. 22).

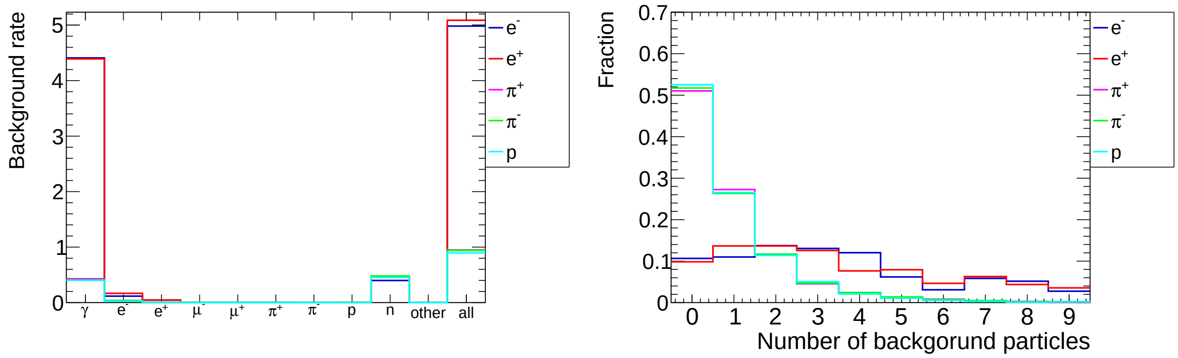

FIG. 20. Background rates per selected tertiary beam particles (left) and the multiplicity distribution of background particles (right). Colors show background distributions for different tertiary beam particles.

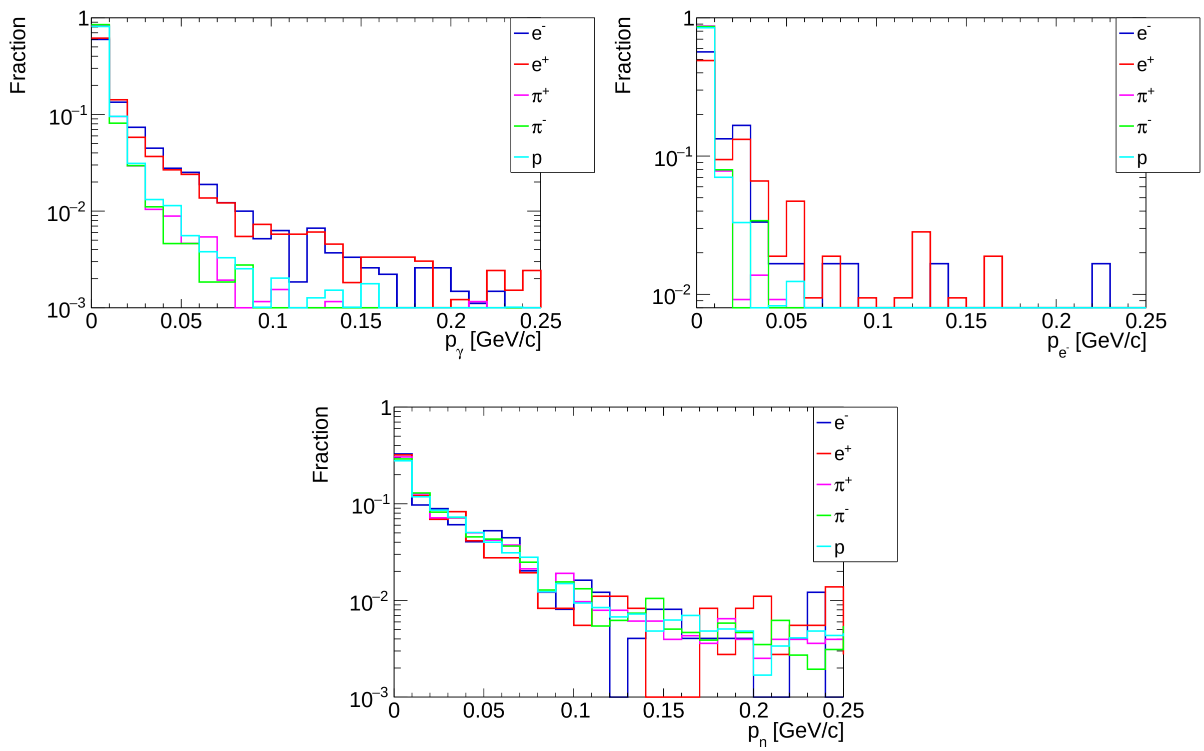

FIG. 21. Momentum distributions of background gammas (top left), electrons (top right), and neutrons (bottom) hitting the tank in coincidence with tertiary beam particles. Tertiary beam particle species are shown in different colors.

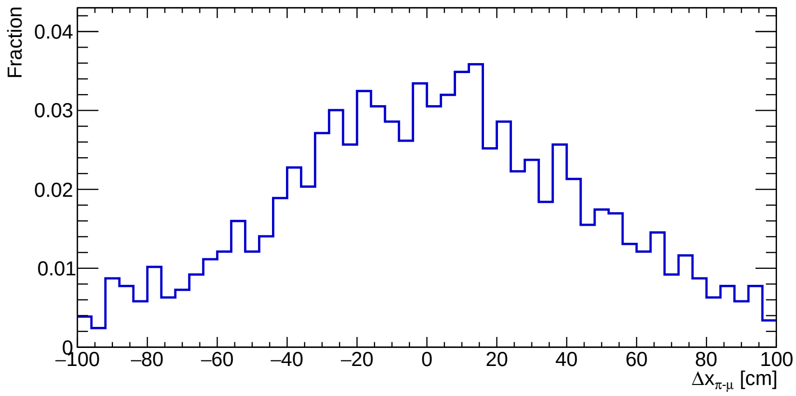

FIG. 22. The difference between muon and extrapolated pion hit positions in the time-of-flight plane placed 1 cm upstream from the water tank. The bin size is 4 cm.

The results of this study demonstrate that it is possible to achieve rates of ~1000 pions per 10^6 incoming beam particles with sufficiently low background rates. Electron and positron rates are lower with higher background. However, electron and positron beams above 0.4 GeV/c can be also obtained from the secondary beam alongside with muons.

Beam particle identification

The particle identification in the beam line is carried out with a combination of time-of-flight (TOF) and aerogel Cherenkov threshold (ACT) detectors. The TOF system will consist of a T0 detector located upstream of the tertiary production target and a large area timing detector located just before the WCTE water tank. For these detectors the acrylic radiator and resistive plate chambers (RPCs) designs used by the EMPHATIC experiment [15] are considered. This system can achieve 100 ps timing resolution. The performance of a 100 ps timing resolution is evaluated in a simple Monte Carlo study assuming 5% momentum resolution from the spectrometer and a 3 m travel distance for tertiary particles. The resulting TOF resolution as a function of momentum for different particle species is shown in Fig. 23. The separation of kaons and protons from other species by TOF is possible over the full momentum range of interest. Electrons can be separated from muons and pions below 350 MeV/c and 450 MeV/c, respectively. The TOF system also has power to separate muons and pions below 300 MeV/c. This may be used to suppress muons from pion decay-in-flight in the tertiary beam configuration if the decay happens sufficiently far enough upstream of the detector.

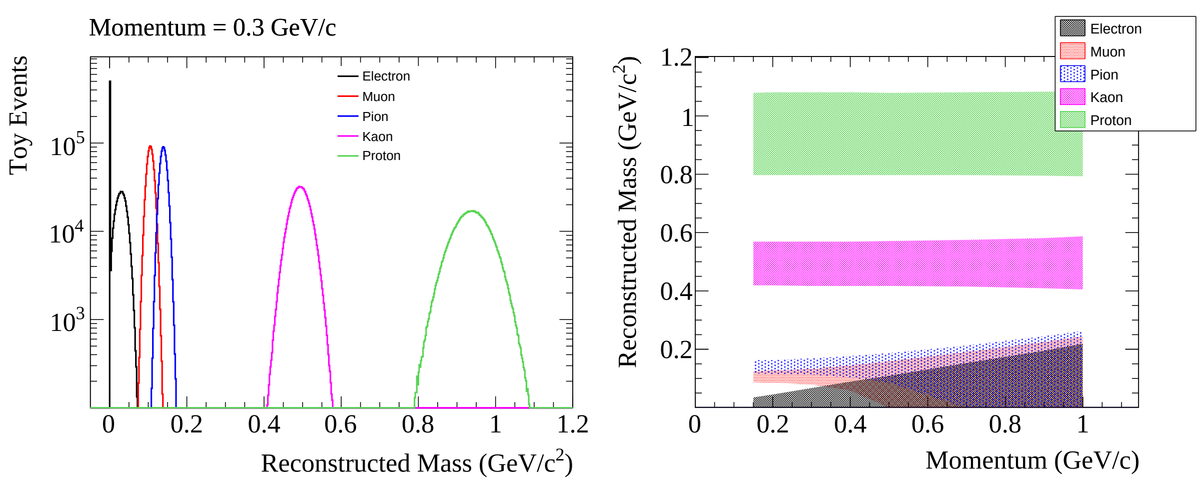

FIG. 23. Left: Expected reconstructed mass distributions for different particle species of 300 MeV/c momentum assuming 100 ps timing resolution. Right: The $\pm 3\sigma$ range of reconstructed mass for different particle species as a function of momentum.

Above 350 MeV/c and 450 MeV/c, additional measurements are necessary to separate electrons from muons and pions respectively. A 1 GeV/c muon has $1/\beta = 1.0056$. Aerogel tiles with refractive indices down to 1.0026 have been produced [16], and these will be used in an ACT, where detection of Cherenkov photons for particles passing through the detector will be used to identify electrons.

B. multi-PMT Photosensors

Single kiloton scale water Cherenkov detectors such as the IWCD are significantly smaller than Super-K and Hyper-K, and therefore faces different challenges in photon detection. Cherenkov photons will typically travel shorter distances from production to detection and so Cherenkov rings will project onto smaller areas. Using the same 50 cm diameter PMTs as Hyper-K would result in poor event reconstruction, especially for multi-ring events and events near the detector wall. These smaller detectors require a finer spatial granularity in order to achieve equivalent sampling. The detector size also necessitates improved timing resolution in order to improve vertex resolution. This is important for defining the fiducial volume and rejecting backgrounds from interactions in material outside the fiducial volume. The photosensors are required to have a transit time spread of ~ 1 ns, which corresponds to a ~ 20 cm light propagation distance.

In order to satisfy these requirements the Hyper-K IWCD will be populated with multi-PMT (mPMT) optical modules, an array of 19 smaller 8 cm diameter PMTs. The mPMT photodetector design is inspired by the spherical modules developed for the KM3NeT experiment [17]. However, the IWCD photosensors will be largely forward facing since they instrument and surround the region of interest inside the detector. Some radius of curvature for the PMT array will be retained so that the individual photosensors have different orientations and image different parts of the detector. This provides directional information about the detected photons which will improve vertex reconstruction. A further benefit to this modular approach is realized in the cabling and waterproofing of the photosensors. An increase in the number of PMTs would typically increase the amount of cabling and waterproofing. Housing many PMTs in a single vessel along with the readout electronics reduces the amount of cabling necessary. Waterproofing and pressure protection are provided by a single vessel for all 19 PMTs housed in the mPMT.

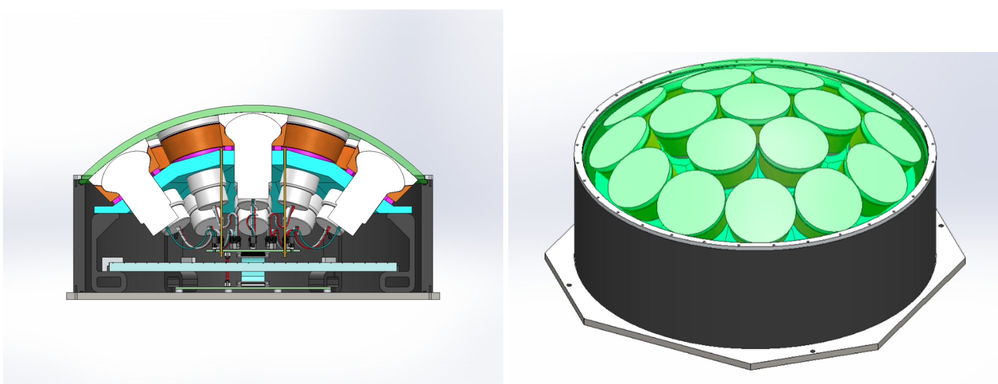

FIG. 24. Left: The cross section view of the mPMT module with 19 8 cm diameter inward-facing PMTs, and integrated front-end electronics. Right: The external view of the mPMT module.

The design of the mPMT module can be seen in Figure 24. An array of 19 8-cm diameter PMTs is supported by a hemispherical support matrix. The PMTs are housed in 3D printed cups which interface with the matrix to fix the orientations of the PMTs. A layer of Poron between the matrix and the cup absorbs compression of the acrylic dome under pressure. The PMTs are optically coupled to the acrylic dome by a silicon gel. Wacker ELASTOSIL RT 604 A/B was chosen because of its optical properties, compressibility, and non-tacky surface. EVONIK UV transmitting PLEXIGLAS GS was chosen for the acrylic dome, which has high transmittance and low levels of Radon emission. Reflector cones are surround each PMT to increase the photocoverage by approximately 30%. A scintillator panel is placed inside the mPMT, improving the efficiency to detect backgrounds having charged particles passing through the mPMTs.

The module is housed in a 50 cm diameter and 16 cm high cylinder closed by a stainless steel plate at the base and an acrylic dome at the top. For the WCTE, the cylinder will be made of PVC, however alternative plastic options are being investigated for the IWCD. In the future, improved versions of the mPMT might be considered for use in Hyper-K.

The WCTE will be instrumented with 128 mPMT modules. mPMT design optimization and performance tests are currently underway. A prototype is shown in Fig. 25. Production of the mPMTs for the WCTE will begin in 2020.

FIG. 25. Top (left) and side (right) views of the mPMT prototype.

C. multi-PMT Electronics

Two essential electronic components of the mPMT module are the high voltage supply and digitization electronics. The former ensures that each PMT gets the correct voltages to produce a signal in response to incoming photons. The considered options involve both the ’cathode grounded’ scheme with anode at positive high voltage and the ’anode grounded’ scheme, with the cathode at negative high voltage. Each has its benefits - the former (and preferable) option provides for a lower overall dark rate, while the latter allows for DC coupling. To cope with the limited budget for power consumption, we cannot use a standard HV supply and a resistive voltage divider. Instead, we have developed an active power supply based on the Cockcroft-Walton voltage multiplier, with PMT dynodes connected to individual taps of the multiplier chain. It is a similar solution to the one adopted in the KM3NeT PMT base design. Revised HV board prototypes have been built and tested. Power consumption of 12.5 mW per channel has been achieved, corresponding to a 237.5 mW of total power consumption for all the HV boards within the mPMT module.

The selected digitization approach for IWCD, as well as the WCTE, is based on full waveform sampling using a FADC. Having access to the waveform provides more information for complicated pulses, and does not introduce dead time. Both are particularly beneficial for the IWCD and WCTE mPMTs, where it is expected that there will be substantial signal rates within the different bunches of the beam spill.

The FADC digitization option for the mPMT electronics is shown in Figure 26. The PMT signals are transformed into differential signals using a transformer and transmitted to the mainboard via a twisted pair flat cable. The same cable is used to transmit HV and slow control signals as well as the power for the PMT base. The differential signals reaching the mainboard are shaped to meet the Nyquist sampling criterion and are then digitized by a 125 MSPS 12-bit FADC. The ADC data is transferred to an FPGA, where digital signal processing (DSP) techniques are used to find pulses and calculate their charge and time arrival. The processed information on each hit is sent from the front-end electronics within the mPMT module to the concentrator card via an ethernet cable. For more complicated pulses, and diagnostic purposes, the raw ADC samples can also be saved. The main electronics board sits on top of a stainless steel base plate which acts as a heat sink.

Each mPMT has a single waterproof cat-5e cable that provides power, clock, sync signals, and a network connection. We expect to have an mPMT Concentrator Card (MCC - Fig. 27) which connects to 24 different mPMTs and provides power, clock and sync signals and communication with the downstream DAQ system. Given the geometry of the WCTE, the MCC will be located outside the tank. While distributing the clock, sync, and power to the mPMTs is straightforward, the collection and routing of the data packets from the mPMTs through the MCC will be more complicated. Options for the data transfer between the mPMT and MCC are being actively evaluated. These include using an Ethernet standard over two pairs (100 Mbit link), replacing the Ethernet physical layer with LVDS link but keeping the protocol part or using custom protocol. The latter - while more time consuming to develop has an advantage of more freedom in choosing the speed of the link as well as encoding clock along with the data, which may allow for two redundant links in a single Cat 5e cable.

D. Data Acquisition Systems

The Data Acquisition systems for the proposed IWCD and WCTE will make use of the ToolDAQ framework. ToolDAQ is a modular and scalable DAQ software system that is planned for deployment in Hyper-K and is used currently by other experiments.

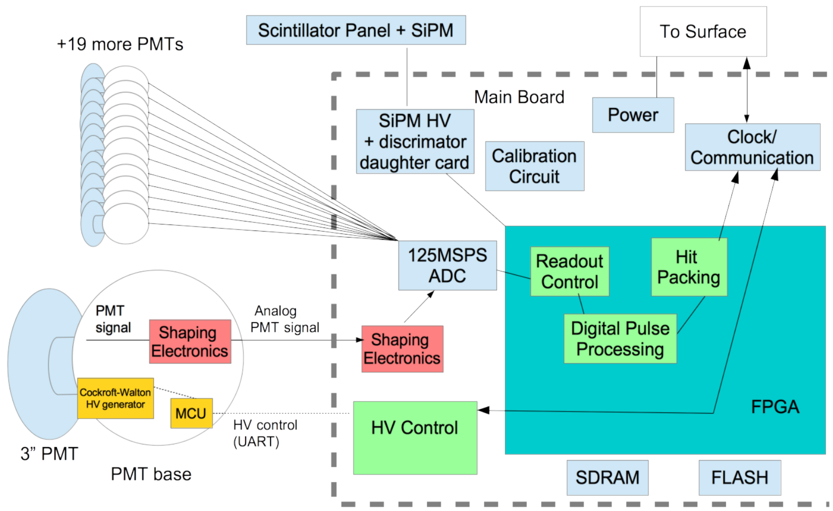

FIG. 26. Block diagram of the mPMT mainboard for the FADC digitization option. The PMT signal is shaped with circuits on the PMT base and mainboard, then digitized with 125 Msps ADC. ADC samples are processed in an FPGA to find pulses and extract the pulse parameters.

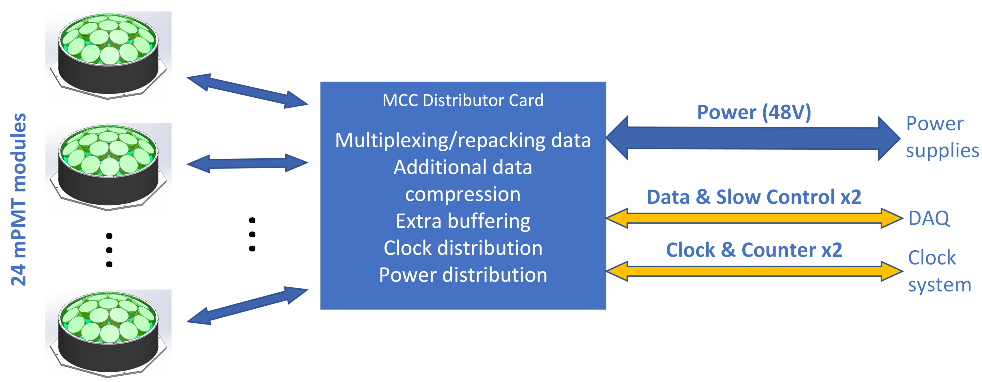

FIG. 27. Connections of multi-PMT to the DAQ with the Multi-PMT Concentrator Card (MCC). The MCC is responsible for distributing clock and power to the mPMT modules and for collecting data from the mPMT modules and sending it to the downstream DAQ system via an optical fiber link.

The 2 x 1 Gbps optical data connections from the MCCs will be connected into two different commercial network switches. This will allow redundancy and the connections will operate as an active backup bonded pair transferring TCP/IP packets to the Layer 3 switches. From here two Readout Buffer Units (RBUs) made from commercial server hardware will also be connected to both of these switches via 2 X 10 Gbps optical links to each switch. The RBUs wll used to buffer and catalogue the hits that are streamed to them from the MCCs. This system can be expanded or reduced depending on the number of MPMTs and MCCs deployed in either the WCTE or IWCD tank and the level of redundancy required. A separate triggering and event building server (TPU/EBU) (with a possible redundant clone) will then be connected to the RBUs to make triggering decisions based on the number of hits seen in the detector over a sliding window and external triggers from beam line or calibration sources. Once a positive trigger decision is made this server will then build and write an event to raided storage installed within it. This configuration can be seen in Figure.28. Event data can then be transferred off site for longer term storage.

E. Slow Control and Monitoring

Slow control and monitoring of the electronics and DAQ will take place via ToolDAQ and be displayed with user interfaces via web pages that will be hosted on either a separate server installed in the experiment hall or the triggering and buffering servers depending on server specs and loading. From here voltages, temperatures, trigger rates, run start

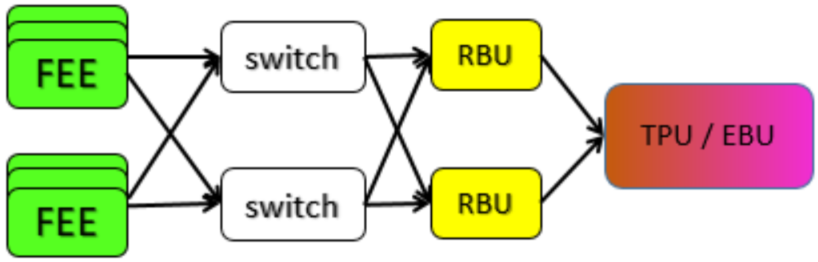

FIG. 28. DAQ schematic for the WCTE and the IWCD. The schematic shows network connections between the front end electronics/ multi PMT concentration cards (FEE), the readout bufer units (RBU) and the triggering processing and event building server units (TPU/EBU)

and stop controls, as well as many monitoring plots of merit will be controlled and commands sent through the DAQ network described above to the relevant MCCs (and on to the MPMTs) or triggering and build servers. Data and run information will also stored in an mirrored SQL servers that will log run configurations start and stop times and other useful information.

F. Calibration Systems

The proposed calibration systems, largely based on the Super-K calibrations [18], include light injectors mounted on the tank wall and deployment of a laser diffuser ball and radioactive sources within the tank. Special consideration is required for the smaller scale of the WCTE compared to IWCD and Super-K, such as smaller/older radioactive sources so as not to saturate the detector. Accurately and precisely understood vertex reconstruction is required to maximize the fiducial volume in such a small detector. Characterizing the detection efficiency also becomes a challenge as most of the active volume is near the edge of the detector, where event reconstruction and particle identification performances vary rapidly over relatively small distances. Finally, to maximize the use of resources and experience, the calibration systems should be designed with consideration of reusing on the movable IWCD.

There are examples of water Cherenkov detectors similar to the IWCD in size ($\sim$1 kiloton), such as Kamiokande, IMB, the K2K 1 kiloton detector, and SNO. Their systematic errors on efficiency are several % or more, which are significantly larger than what is required for IWCD (1-2%). This is one of the most challenging aspects of IWCD and a critical point for the success of the Hyper-K project. The SNO experiment did the most precise measurement among the small water Cherenkov experiments by controlling their efficiency error to the limit of uncertainties in the angular responses of PMTs and the positions of each PMT in the vessel, which are tightly related. Thus, in addition to the calibration sources similar to Super-K, the IWCD will attempt geometrical calibration by photogrammetry and ex-situ calibrations of PMT angular response at photosensor test facilities (PTFs). To help address these challenges, additional systems are also being considered. Each mPMT will contain a pulsed LED to monitor timing parameters and steady LEDs to define fiducial markers.

In order to calibrate physics processes, such as the response to hadron interactions and light scattering in the detector, a test beam of known particle types and momenta is required. The WCTE will establish state-of-the-art calibration systems and procedures for small water Cherenkov detectors and provide the necessary physics measurements to understand the production of Cherenkov light by charged particles in water.

Calibration sources and deployment system

The primary calibration source for the WCTE will be a laser diffuser ball, similar to that used by the SNO and DEAP-3600 collaborations [19]. This will provide uniform mono-chromatic light with a sub-nanosecond pulse width and of sufficient intensity to calibrate the time response of the mPMTs. The source will also provide uniform low-intensity pulses that will illuminate the PMTs at the single photon level, allowing *in-situ* PMT gain calibration. The deployment system considered for the IWCD and WCTE is a manipulator arm deployed from the top of the tank, a conceptual design of which is shown in Fig. 29. The deployment system will position the diffuser ball at various positions in the detector, allowing a detailed study of the detector optical properties near the edge of the fiducial volume.

The deployment system will have a central bore of between 90 mm and 150 mm. This will allow the diffuser ball to be removed and replaced with a radioactive source. As a result, the same system will be able to move a radioactive source to any point within the tank to provide detailed information on the mPMT efficiency and single photo-electron gain. As

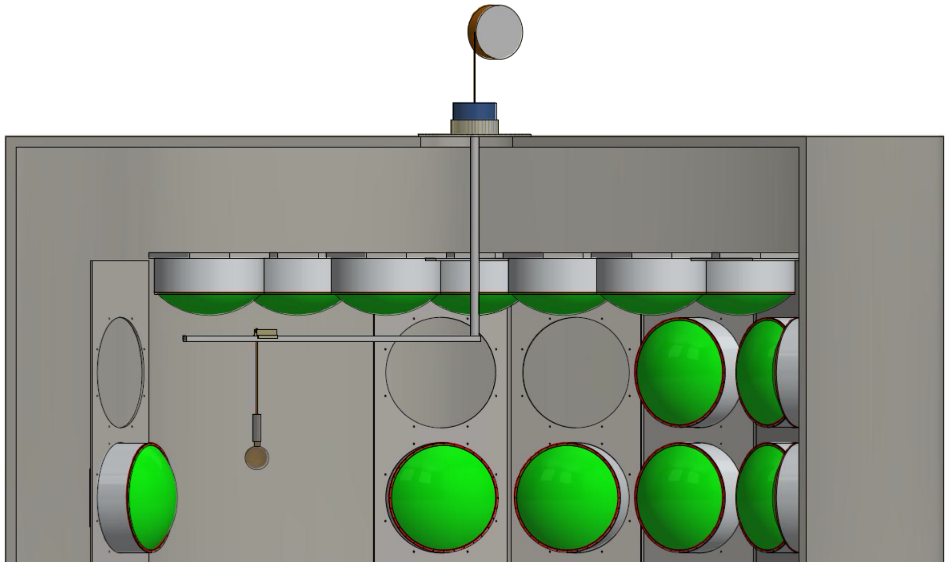

FIG. 29. Conceptual design of calibration source deployment system, with mPMTs on the back wall of the detector removed for clarity.

discussed above, the radioactive source activity will have to be lower than that used by Super-K. The source will also have to be stored appropriately when not in use.

Geometrical calibration using photogrammetry

An incomplete understanding of the *in-situ* photosensor position limits the precision of the final event reconstruction. Sensor position uncertainties arise from the support frame shifting due to sensor buoyancy and water pressure. This displacement was as large as several cm for SNO, and the distortion of the tank was apparent by eye in the case of the K2K 1 kiloton detector. SNO+ developed a new technique of measuring the PMT positions using photogrammetry [20]. Photogrammetry will pinpoint the position of each sensor by deploying underwater cameras, taking multiple photographs of the detector, and performing stereoscopic reconstruction.

For the WCTE, we will affix two to four ~ 40M pixel mirrorless digital cameras in underwater housings to the mPMT support structure. An additional $\sim$120M pixel and/or 360 camera will be deployed with the source deployment system, providing pictures of the detector at various positions and angles. By fitting the images, a 3D image of the inner surface of the detector can be reconstructed that will be millimetre level precision.

mPMT calibration with embedded LEDs

The ability to monitor and correct any timing offsets between individual PMTs is essential for the detector. A method to do this has been investigated using LEDs embedded into the mPMT module. An LED would excite a fiber that ends near the the center of the mPMT, as shown in Fig. 30. The LED would be driven at a high intensity by a pulsed source, sending light throughout the WCTE tank to illuminate many other mPMTs. A prototype driver circuit has leading edge jitter of less than 0.1 ns, much smaller than the transit time spread of the PMTs.

Assuming each mPMT is equipped with a flashing LED one can compare the expected arrival time of LED light to the measured arrival time for all possible combinations of LED and PMTs. Minimising this with respect to possible time offsets between PMTs allows one to constrain these time offsets. Simulation studies have shown that this system can achieve a 0.1–0.2 ns precision on the time offsets for each PMT when used in the WCTE detector, without needing to deploy special calibration equipment.

The system provides two other benefits. First, the red LEDs shown in Fig. 30 can provide a constant illumination that can be used for the photogrammetry discussed above. Second, because the PMT timing offsets are accurately known, a flashing LED affixed to deployed calibration sources can be used to locate the source within the detector in real time with mm precision. This method can be cross checked with the photogrammetry approach to understand any limitations with these systems.

FIG. 30. Front-face of the mPMT showing the location of the pulsed LED (blue) and the constant LEDs (red).

Ex-situ calibration of photosensor angular response

The angular response of each photosensor can be a significant source of systematic uncertainty, in particular when it is coupled with displacement of the photosensors. Photosensor test facilities (PTFs), like the one currently operating at TRIUMF, can illuminate the surface of a PMT at a specified angle and position using a laser-equipped motorized gantry. A second gantry can be used for characterizing reflections from the PMT surface or other detector materials. The PTFs will provide detailed maps of the angular and position response and reflectivity of the multi-PMTs used in the WCTE.

Natural Particle Sources

Additional particle sources arise from cosmic muons and the Michel electrons from those that stop in the detector. A summary of the energy scale calibration obtained from these sources in Super-K is shown in Figure 31, including the difference from MC of the means of the Michel spectrum, muon momentum/range distributions, and neutral pion mass. The imperfect agreement at the $\sim 2\%$ level enters as a systematic error and limit the precision of high level neutrino oscillation analyses.

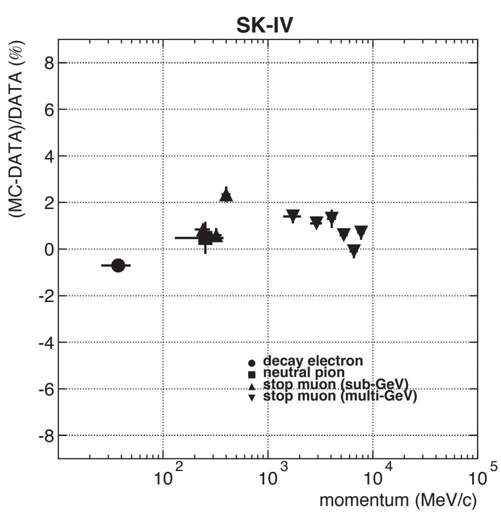

FIG. 31. Measurements of the absolute energy scale in Super-K compared to MC with various high energy particle sources.

In order to improve this and achieve a 1% level total systematic error, a detailed understanding of the detector must be established using fundamental physics parameters such as water scattering and absorption, material reflectivities,

TABLE III. Non-exhaustive list of fundamental physics parameters that affect and thus can be constrained by, to first order, the various calibration sources and measurements.

Systematic Parameter	Light Injectors, Diffuser Ball	Radioactive and Particle Sources	PMT Test Facilities	Photo-grammetry	CERN Beam
Geometry	✓	✓		✓	
Water	✓	✓			
Reflections	✓	✓	✓		
Timing	✓	✓			
PMT Response	✓	✓	✓		
Cherenkov Physics		✓			✓

TABLE IV. List of calibration sources and experiments they have been/will be deployed at. This table only includes sources deployed at the experiment, and only those sources that will be used at WCTE. Parentheses indicate differences between sources at experiments. The Super-Kamiokande and Hyper-Kamiokande diffuser balls can only be deployed down fixed vertical lines. The neutron source will only be deployed for WCTE and IWCD provided the detector contains gadolinium. Photogrammetry can be performed with fixed cameras in WCTE/IWCD, while Super-K/Hyper-K would require ROVs.

Calibration System	Super-Kamiokande	WCTE and IWCD	Hyper-Kamiokande
Light Injectors	✓	✓	✓
Diffuser Ball	(✓)	✓	(✓)
Nickel Source	✓	✓	✓
Neutron Source	✓	(✓)	✓
Photogrammetry	✓	(✓)	✓
mPMT LEDs		✓	✓
Muon tracker		✓	

PMT time and charge responses, detector geometry, and so on. This model should be able to describe every calibration source and data set such that any data/MC discrepancies can be understood via reasonable tuning of parameters. Then, a charged particle beam will provide a sample of particles with known energies that span the range of interest for IWCD and Hyper-K, that can help understand the systematic discrepancies in e.g. Figure 31. Furthermore, the WCTE will provide essential data by filling in the gaps where natural particle sources cannot probe.

Table III summarizes the calibration sources and measurements described above, together with the known fundamental parameters affecting such measurements. Ideally, one could design calibration sources or measurements that diagonalize this matrix, however, in-situ measurements necessarily convolute most of the parameters and suffer from several degeneracies. Ex-situ measurements, such as the PTFs, or photogrammetry help to disentangle some parameters, but several independent light and particle sources will be needed to fully constrain the problem for a robust and precise measurement of the Cherenkov physics with the test beam.

Table IV identifies the different calibration sources that will be deployed at WCTE and IWCD, and indicates whether they have been used (or will be used) at the Super-Kamiokande and Hyper-Kamiokande detectors. The *ex-situ* calibrations have not been included, but are performed for all experiments.

G. Water System

Super-Kamiokande has a diagonal dimension of ~ 50 m and an attenuation length for visible photons of ~ 100 m. To ensure that the fractional attenuation of photons in the WCTE is equivalent to or less than in Super-K, an attenuation length of ~ 11 m or better should be achieved in the WCTE. However, it is also of interest to operate the WCTE with an attenuation length to particle path ratio significantly larger than Super-K so that the effects of reflections and high-angle Cherenkov light production can be separated from photon scattering in the detector.

Super-K achieves ultra-pure water with a system that includes microfiltration filters, degasifiers (vacuum and/or membrane type), reverse osmosis membranes, deionization resins, and exposure to intense ultraviolet light. The water flow rate in Super-K is $\sim$60 ton/hr. The IWCD detector will use a two-stage water system. For initial filling, reverse osmosis membranes and electrodeionization will be used to purify the water. Ultra-pure water will be achieved and maintained by a final polishing unit that uses ultraviolet light, deionization resins and microfiltration. The water flow rate for the IWCD is 5 ton/hr.

The WCTE has 10% of the total water mass of the IWCD, so it may be assumed that a 0.5 ton/hr flow rate is sufficient. However, it is expected that leaching from the PVC cylinders used in the mPMTs is a dominant source of impurity in the IWCD and WCTE. Since the WCTE has 27% of the number of mPMT in the IWCD, we will use a system with 2 ton/hr flow rate to ensure sufficient purity in the WCTE. The 2 ton/hr flow rate also allows a turnover time of ~ 1 day, so that after any changes to the water system, equilibrium can be achieved quickly, minimizing wasted time during the operation phase of the experiment.

If a deionized water source at CERN can be used to fill the tank, than a commercially available final polishing system will be sufficient for the WCTE. An example unit that can provide 2 ton/hr Organo FP-2000-UF. This unit has a footprint of 1.55 m$\times0.7$ m and maximum power consumption of 3.1 kw. If deionized water is not available at CERN, then it will be necessary to install reverse osmosis and deionization systems for initial tank filling. Commercially available modules that can provide 2 ton/hr flow rate will take up an additional 3 m$\times$1 m of floor space and consume up to 20 kW. However, these will only need to be operated during the initial filling stage.

It is planned to have a phase of operation with loading of $Gd_2(SO_4)_3$ at a concentration of 0.2% by mass, the same concentration planned for Super-K. Operation with $Gd_2(SO_4)_3$ will require modifications to the water system. The EGADS collaboration has developed, a molecular band-pass filter system is used to remove impurities while keeping the dissolved Gd in the water [21]. This system could be adapted to the WCTE, however alternative approaches are possible. Organo now has the capability to produce specially treated resins that do not remove dissolved $Gd_2(SO_4)_3$. These resins can replace the resins typically used in the final polishing system and the remainer of the water purification system can remain unchanged. This approach is planned for the WCTE The removal of $Gd_2(SO_4)_3$ after the Gd phase is complete requires the use of expensive deionization resins. Hence the run plan for the WCTE will only include a single Gd operation phase.

H. Tank and Support Structure

To maintain material compatibility with ultra-pure water and Gd-loaded water, stainless steel 304 will be used for construction of the tank and support structure for the photosensors. Fig. 32 shows drawings of the mPMT support frame with and without mPMTs mounted. mPMTs in the barrel region and top end cap are mounted from outside of the frame. The mPMTs in the bottom end cap are mounted from inside the frame. The assembly procedure is to first assemble the bottom end cap and barrel of the support frame outside of the water tank. The mPMTs are then mounted on the bottom end cap and barrel of the support structure. The mPMTs are mounted on the top end cap before it is installed on the top of the support frame using a crane and bolted into place.

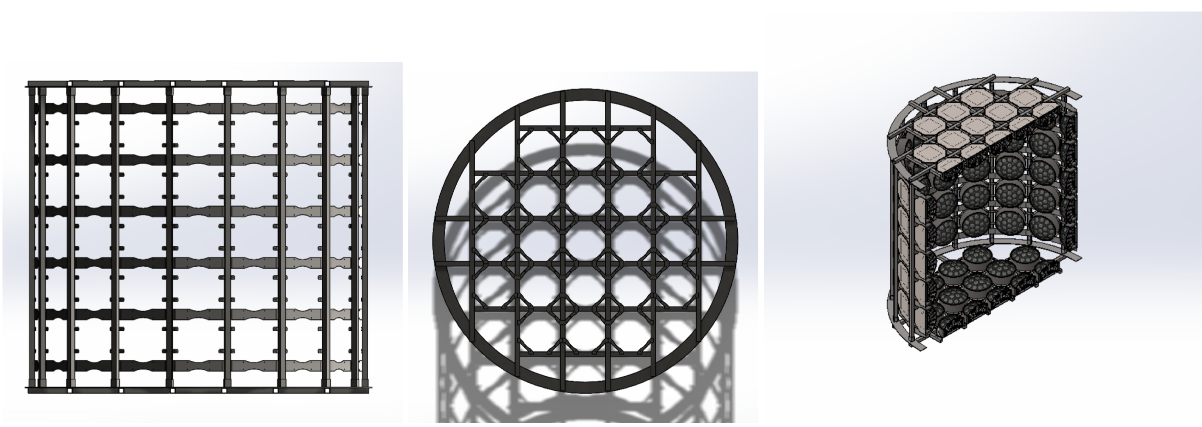

FIG. 32. Drawings of the WCTE mPMT support frame. Left: A side view of the barrel region. Middle: A top view of the bottom and top end caps. Right: A cross section view of the support frame with mPMTs mounted.

After the support frame and mPMTs are assembled, the total mass is ~ 8 tons. This assembled structure is moved by crane into the water tank. The water tank has a 4.1 m diameter, 4 m height and 6 mm thick walls. Fig. 33 shows the external view of the tank and a cross section view highlighting the method to deploy calibration sources. The top of the tank has a flange the provide both structural support and a surface on which the tank lid is sealed and bolted in place. The tank lid includes ports for calibration source deployment (at the center), water circulation, cable routing and cover gas circulation. A cover gas of N_2 or CO_2 free air is circulated to maintain the water quality. The bottom of the tank is supported by the floor in the experimental area. The tank will be installed on hard rubber mats to ensure even distribution of the weight to the floor.

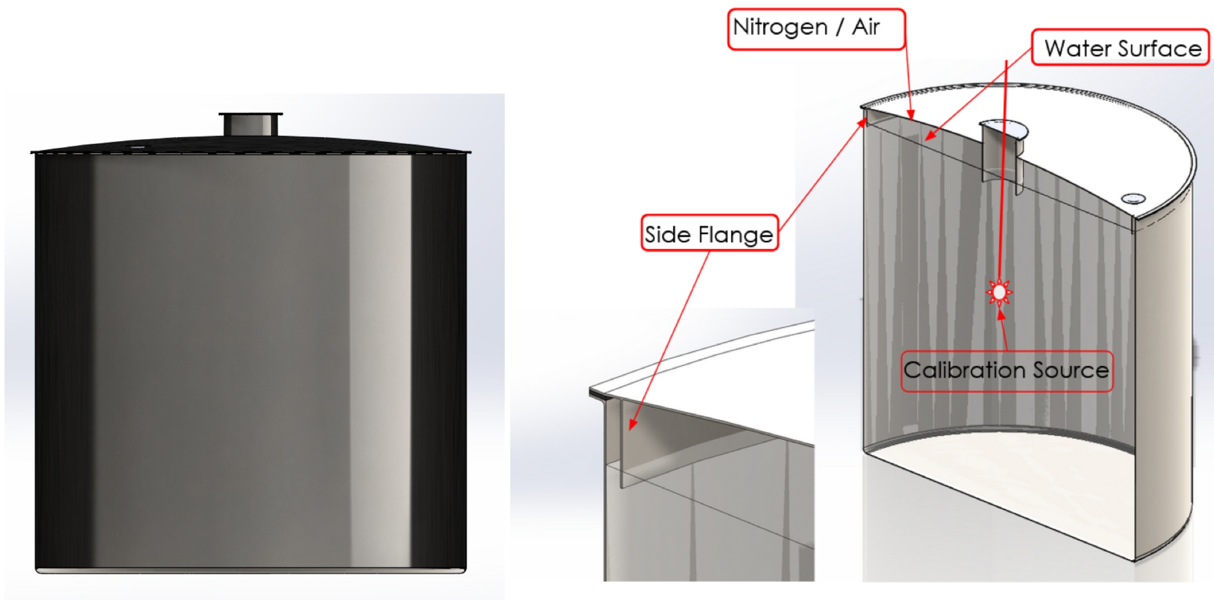

FIG. 33. Drawings of the WCTE tank. Left: Outside view of the tank with lid installed. Right: cross section view of the tank showing the method of calibration source deployment through the center port in the lid.

Fig. 34 shows more details of the tank lid and its ports. The tank lid is sealed to the tank with a rubber gasket to avoid leaking of the CO_2 free cover gas. The center calibration port is 50 cm diameter. The mPMT slot below the calibration port will be empty so that calibration sources can be deployed into the tank. Two workers on top of the tank will carry out the deployment. The tank will be fitted with a ladder to access the top, and a railing will be installed around the edge of the lid to protect against falls. A dark tent will be installed over the calibration port during deployment to avoid light leakage into the detector. Water is circulated through two 2.5 cm inner diameter pipes that enter the tank through the port at the side of the lid. One pipe is routed to one side of the bottom of the detector, while the other pipe is routed to the opposite side of the top of the detector. The pipes are used for water inlet and outlet. Ports are also available for the cover gas circulation. The mPMT cables will be routed to single point, bundled and fed through another port in the lid.

The WCTE tank has two beam windows for the secondary beam and the tertiary beam (Fig 35). The secondary beam can be confined in the smaller beam spot of less than 100 mm in diameter. The extendable beam window is adopted for the secondary beam window to simulate the particles starting inside the tank. The extendable window consists of two parts, a flexible waterproof hose with a extendable rigid pipe inside (Fig 36).

The tertiary beam window is 500 mm diameter(Fig 37). The window flange is directly welded onto the tank.

Numerical simulation is performed for the support structure resting on bottom with top endcap without water, which is the case with highest stress on the support structure (Fig 38). The fixed support is applied on the bottom face of the bottom end cap. Weight of each mPMT is 40 kg and 400 N force is applied at the respective locations of the mPMT's. The maximum equivalent stress is 65.89MPa at the bottom endcap ring, and the maximum total deformation is 1.045mm at the centre of the top endcap.

The support structure will be assembled in the assembly hall at CERN. Fig. 39 shows the assembly procedure of the WCTE detector. The assembly procedure starts with placing the prefabricated bottom end cap and then aligning the split barrel side column as shown in the second step. Continue the same procedure for all four parts of the barrel part and establish a proper connection using the connecting plate. Mount pipes for water circulation system, camera and lights for photogrammetry, and mPMT modules on the bottom end cap. The next stepis to mount the mPMT's on the barrel of the support structure with crane and scaffolding. The structure loaded with mPMT's will be lifted into the tank. It should withstand the load of mPMTs while mounting and lifting. After ensuring the support structure is properly seated on the tank, the secondary beam window will be installed as in step 7. The assembly of the top end cap which consists

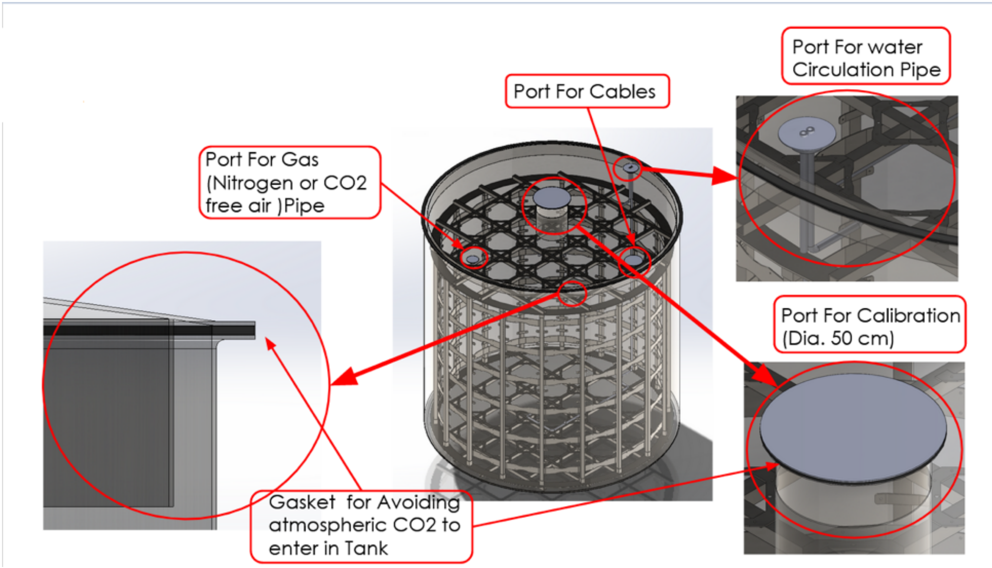

FIG. 34. Drawings of the WCTE tank and lid highlighting the sealing of the lid and the ports in the lid.

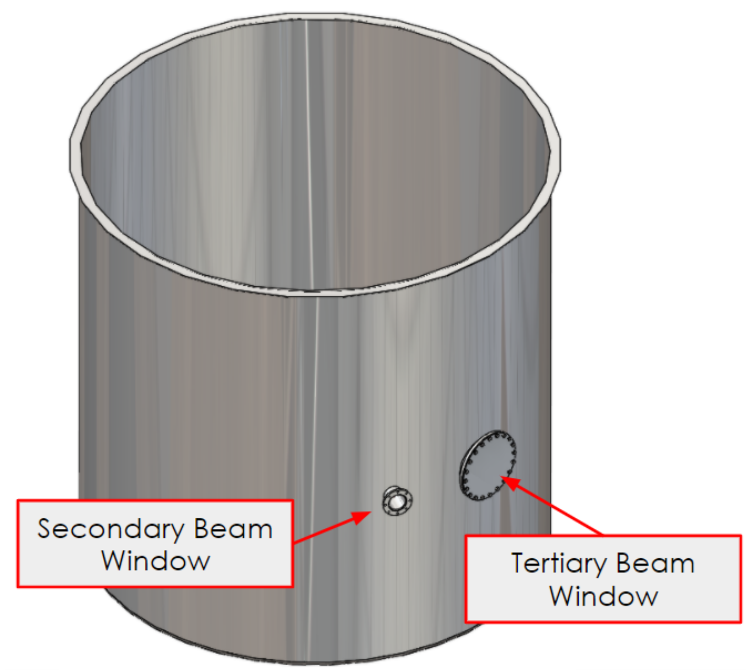

FIG. 35. WCTE beam windows on the tank.

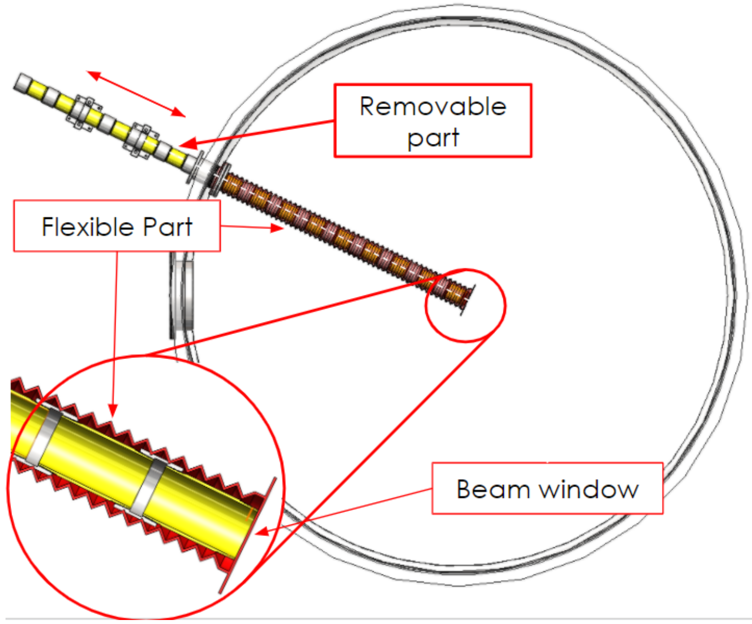

FIG. 36. Schematics of the extendable secondary beam window.

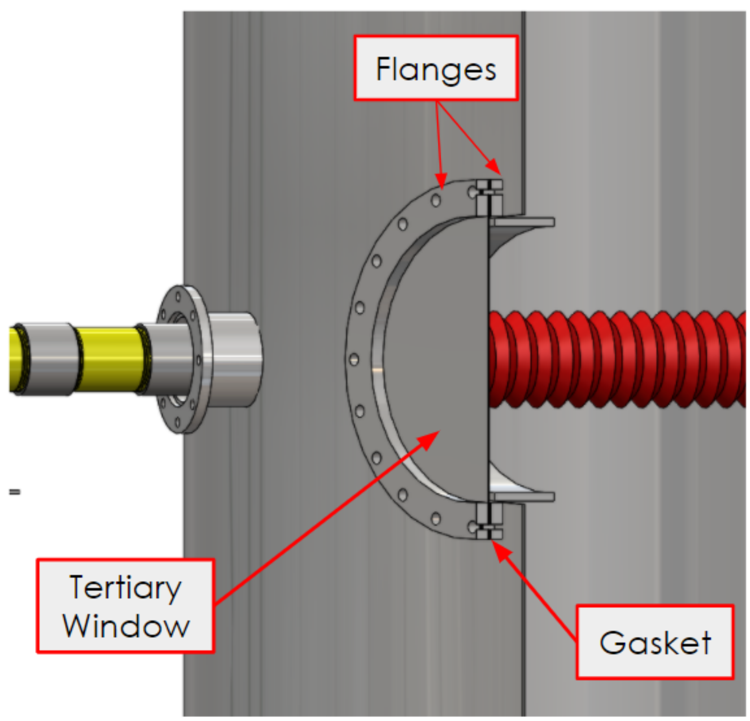

FIG. 37. Tertiary beam window.

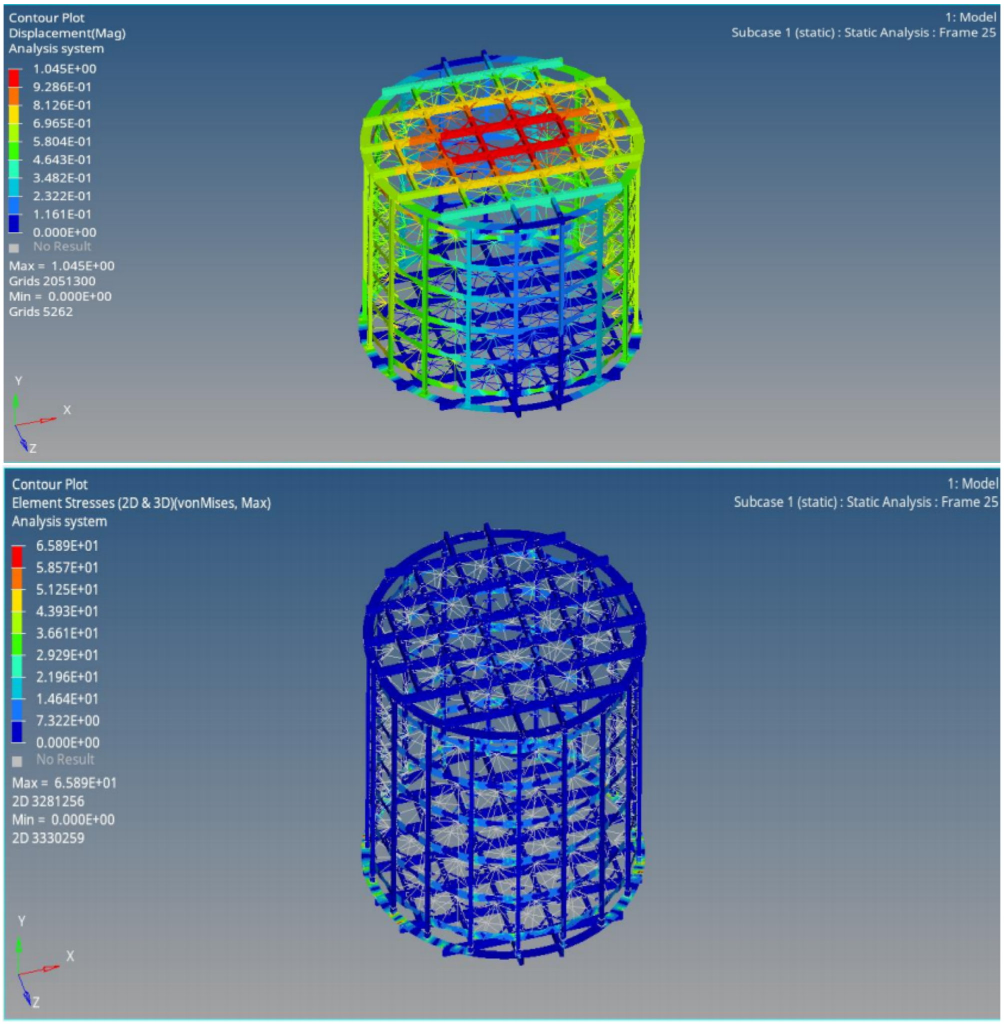

FIG. 38. Numerical simulation of the mPMT support structure.

of the mPMTs, calibration arm, and camera and light system for photogrammetry is done on an elevated platform as shown in step 8. Then the assembled top endcap will be moved onto the barrel section using a crane with a lifting beam. Finally, the top lid is attached to the barrel part using clamp and nut and bolts to ensure proper connection with sealing gasket to seal the cover gas in the detector. After assembly of the detector, it will move to the experimentation hall.

I. Experiment Layout

The layout of the WCTE experiment in the T9 experimental area is shown in Fig. 40. The detector is positioned away from the axis of the secondary beam to avoid secondary particle flux in the detector and to allow for the detection of tertiary particles produced at an angle of $\sim$450 mrad. Shielding on the downstream side of the detector blocks back scattering from the downstream shielding of the T9 area.

The height of the beam above the floor is 1.4 m. The ideal entry point of the beam in the WCTE is $\sim$2 m above the floor. However, the floor blocks can be moved to lower the WCTE by 0.8 m, centering the beam on the WCTE.

When running in the muon configuration, the target for tertiary production will be removed. In order to aim the beam at the detector it will be necessary to move the detector and spectrometer into the T9 secondary beam line. This will be achieved by partially draining the WCTE tank so that the detector can be moved by the 40 ton crane in the experimental area.

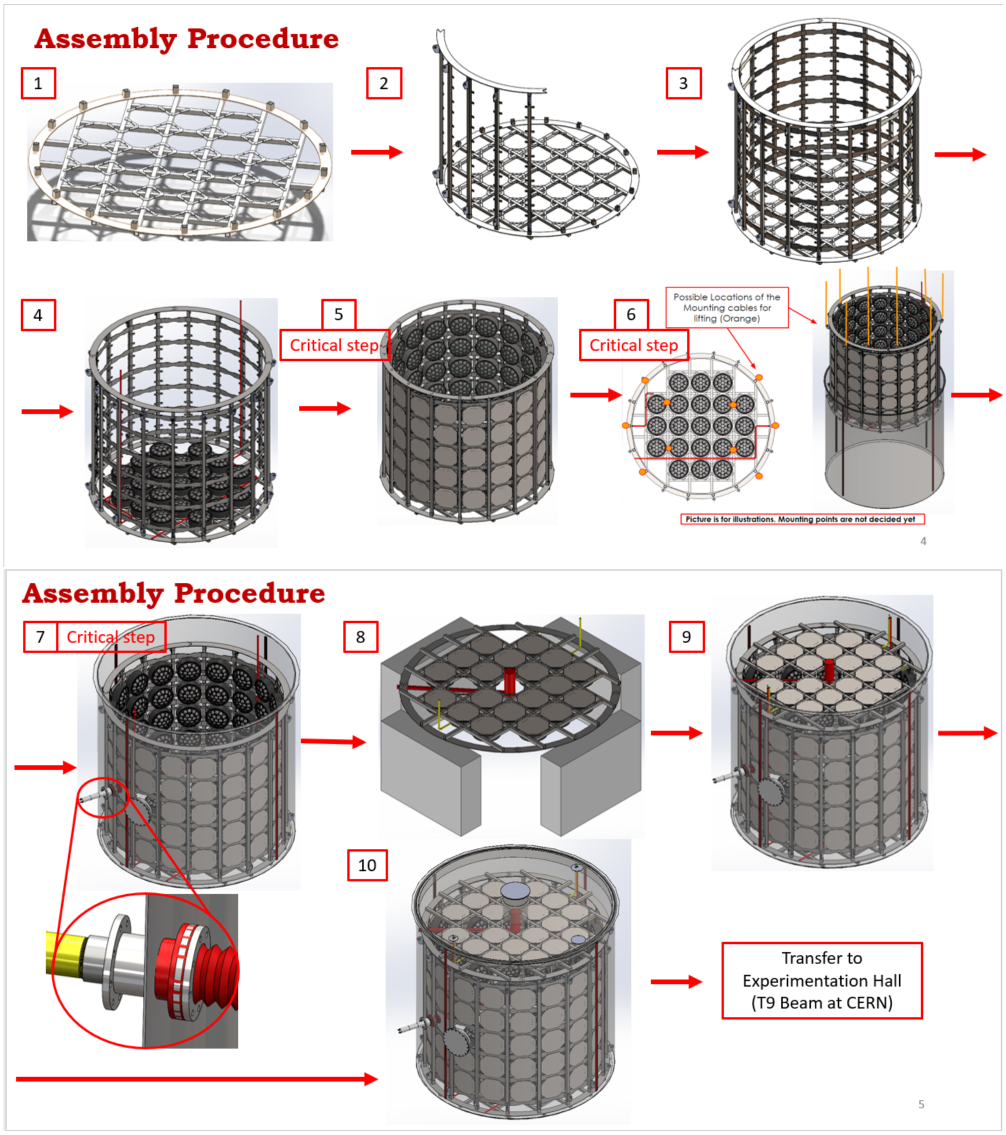

FIG. 39. Assembly procedure of the WCTE detector.

J. Moving the detector between the tertiary and secondary beam configurations

The WCTE detector needs to move between 3 to 4 linear meters across the T9 room, as shown in Fig. 40. The movement from tertiary to secondary beam line may need to be repeated during the WCTE experiment, and for the purposes of the design of the movement system the tank is to remain at full mass, and none of the major elements of mass will be removed (i.e. the water).

Tank Properties

The approximate dimensions of the tank are shown in Fig. 41 (left). The mass of the tank and its major components are shown in Tab. V and a diagram of the components is in Fig. 41 (right).

Proposed moving system

A preliminary design of the detector moving system has been prepared by CERN engineer Pierre Minginette and the design has been updated by the WCTE collaboration to fit into the T9 experimental area. The transition of the detector from tertiary to secondary beam position is to be done by a set of mechanical rollers moving along a rail system. The

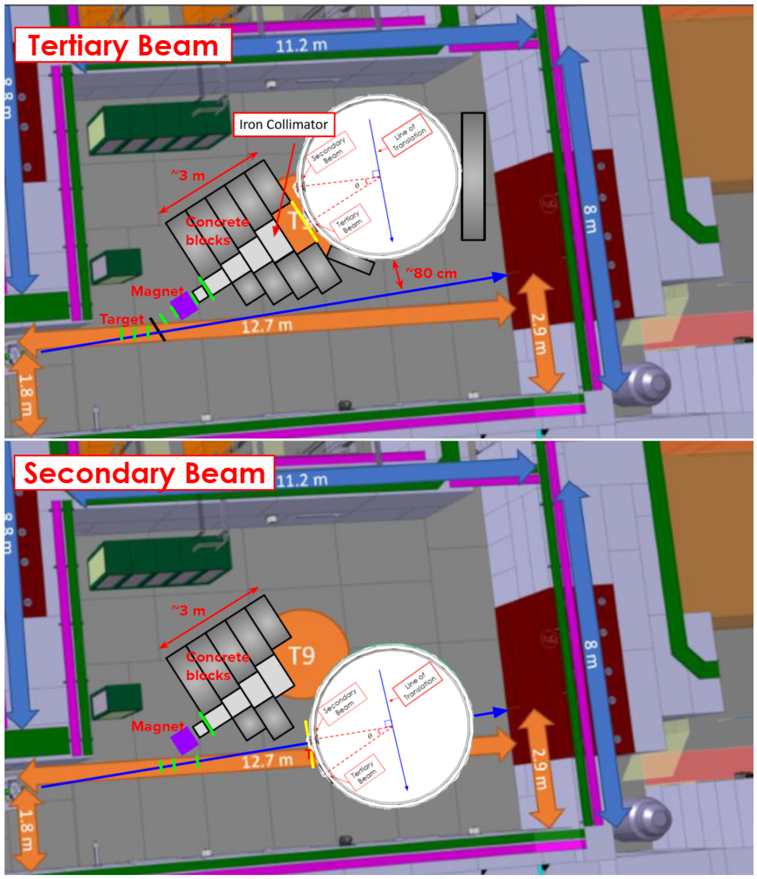

FIG. 40. Layout of the WCTE in the T9 experimental area.

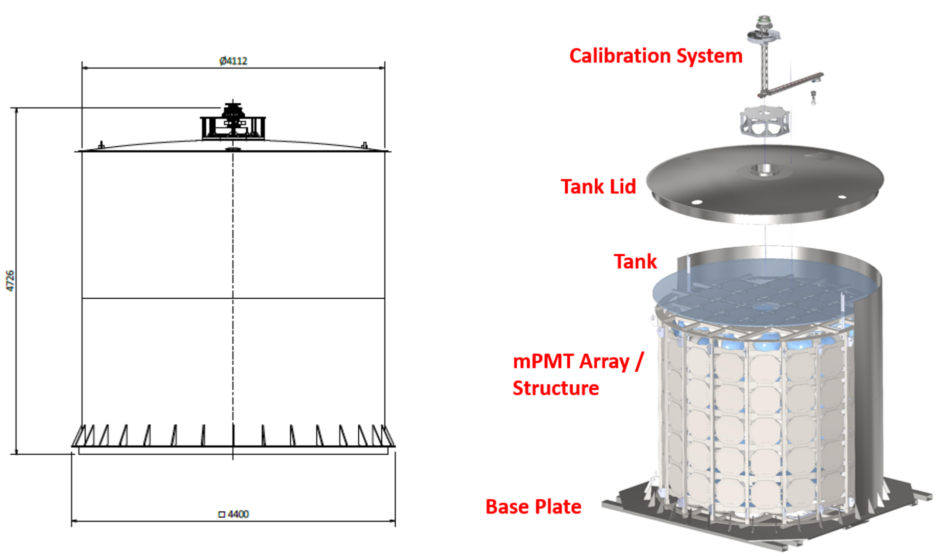

FIG. 41. The approximate dimensions of the WCTE tank used for movement system discussion (left) and the diagram of the components (right).

Component	Mass (kg)
Tank	2,400
Base	3,100
Lid	750
Water	52,500
mPMT Array	10,000
CDS	120
Total	68,870

TABLE V. Breakdown of the tank mass used for movement system discussion.

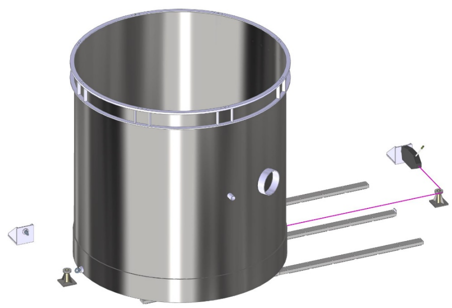

FIG. 42. Drawing of the tank moving system, consisting of a roller system on three rails and a wire rope puller.

force to move the ~70,000 kg is to be generated by a manual 'wire rope puller'. Fig. 42 illustrates the detector mounted on 3 rails, when in the tertiary position. At either end of the rails are a pulley and anchor point.

A floor mounted bracket, that is fastened to the concrete foundation by specialist bolt, provides the position to which one end of the wire rope is attached. A hand operated wire rope puller with a telescopic leaver is used to mechanically pull the wire rope through the device, keeping a tension on the rope and pulling the detector along the rails. A feed pulley bolted to the concrete foundation allows the wire rope direction to be rotated by 90 degrees so that the system fits inside the T9 experimental area. These systems are illustrated in Fig. 43.

Three steel rails, each 150 mm wide by 60 mm thick, are bolted to the floor of T9. Three skates are installed on each rail, giving nine skates in total that support the detector and its movement. Each skate has cylindrical rollers that move

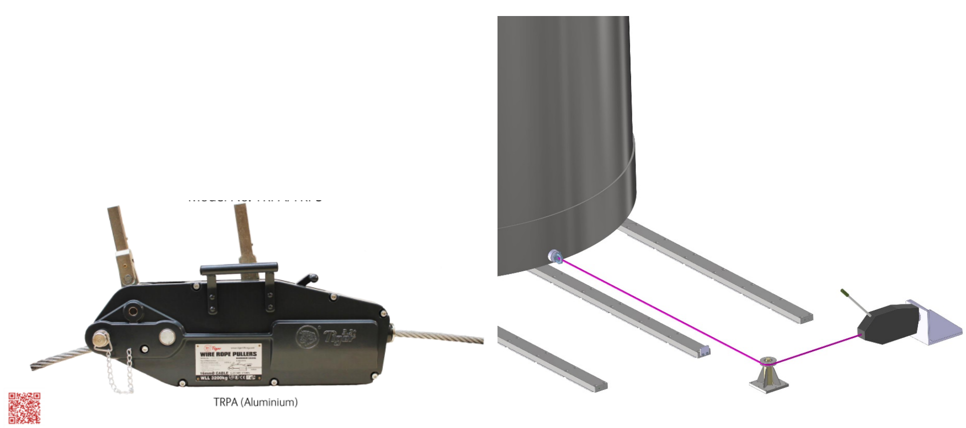

FIG. 43. Example wire rope puller (left) and drawing of the system with the feed pulley and wire rope puller (right).

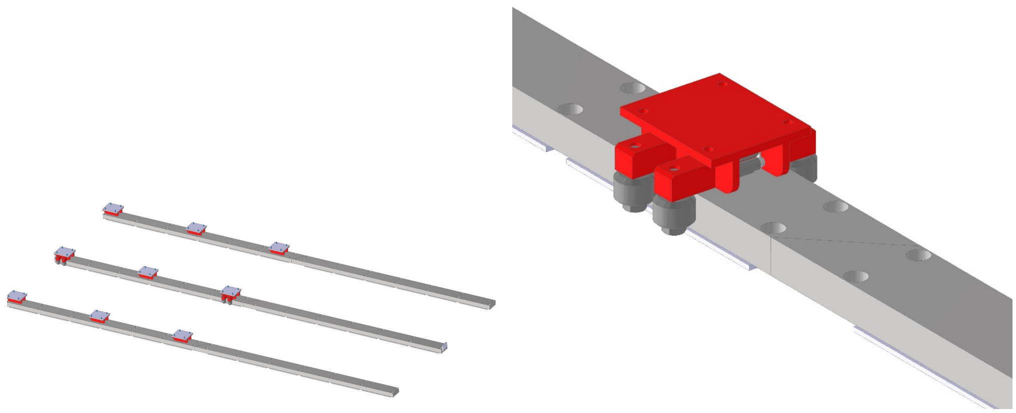

FIG. 44. Drawing of the rails (left) and skates (right) for the moving system.

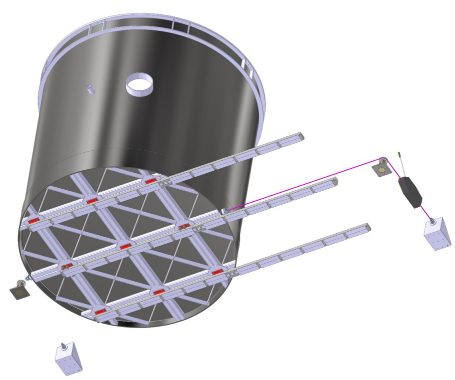

FIG. 45. View of the detector moving system from the bottom.

over the rail, bearing the weight of the detector, and cylindrical rollers on the side of the rail that ensure the linear motion in the desired direction. Drawings of the rails and skates are shown in Fig. 44.

Fig. 45 shows the underside of the detector. The skate positions can be seen affixed to the detector vessel by means of a reinforce steel fabricated structure, with cross beams to strengthen the underside of the vessel. There is a fixed point at the base of the detector and a 16 mm diameter wire rope is connected at this point as shown. The wire rope passes around the pulley and into the rope pulling machine, which is in turn connected to the anchor point. When the lever on the rope puller is operated the wire is pulled through the system and thus the detector vessel moves along the rail.

Analysis of the detector moving system

Pierre Minginette has performed a static analysis of the detector moving system, including the framework at the bottom of the tank that sits on the skates and rails, and the anchors used in the pulling of the detector.

For the analysis, a water volume of 50.5 m^3 is held inside the detector, and the detector is mounted on the skates of the moving system. Fig. 46 shows the distribution of load over the fabricated framework on the underside of the detector. A maximum load of 41.2 MPa is generated at the centre of the vessel floor, and the load is evenly distributed across the reinforced base of the detector vessel, and across the 9 mount points for the moving system skates. The maximum deformation is also evaluated, as shown in Fig. 46, and found to be 2.1 mm.

The barrel of the detector is subject to 0.4 MPa of hydrostatic pressure at the top of the detector, and a progressive increase of pressure as the water pressure builds over the 4 m depth, until a maximum of 12 MPa is reached near the connection point of the barrel to the bottom floor of the vessel, as shown in Fig. 47. The maximum deformation of the barrel in the horizontal direction is 1.8 mm, as shown in Fig. 47.

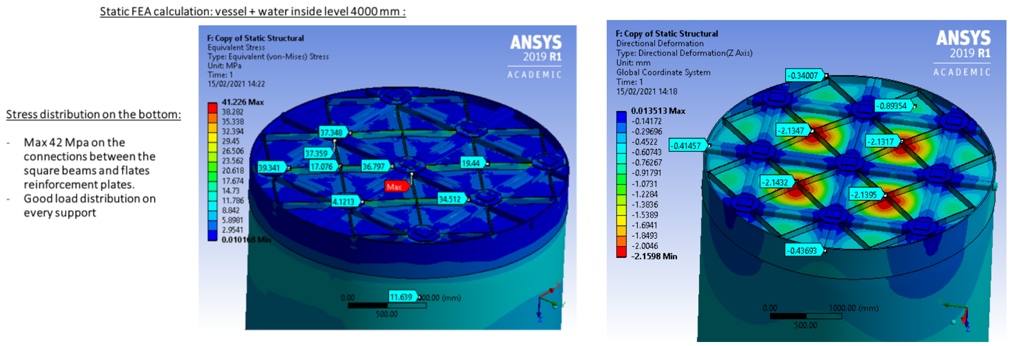

FIG. 46. Results from the analysis of the structure at the bottom of the tank showing the load (left) and displacement (right).

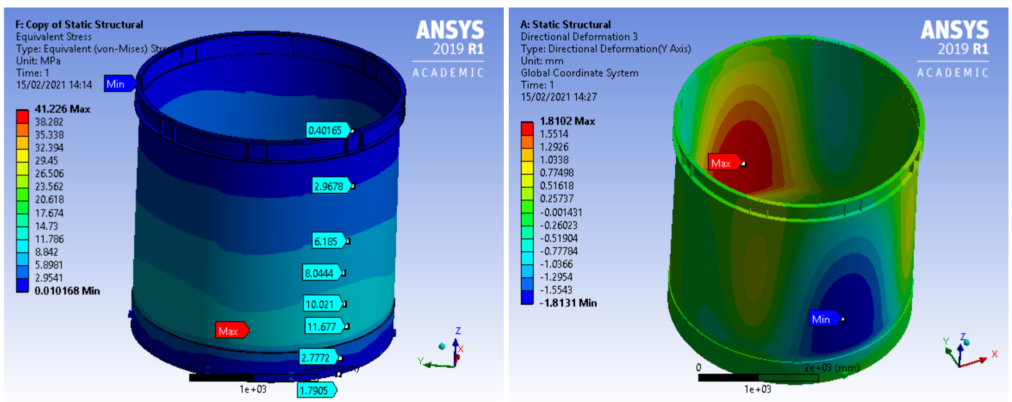

FIG. 47. Results from the analysis showing the distribution of pressure (left) and displacement (right) on the tank.

The traction force exerted on the anchor point and the tanks itself is shown in Fig. 48. The force acting on the detector tank produces a 0.6 mm deformation in the vessel as it is being moved. The anchor point to which the hoist system is fastened is subject to 140 MPa and a deflection of 0.5 mm.

In conclusion, the framework on the underside of the detector evenly distributes the load of the water, with an even distribution of said load on each skate. The loads on the underside and tank wall are acceptable for the grade of stainless steel used at the thickness of 6 mm. The moving system is under acceptable levels of stress for each of the fabricated anchor points.

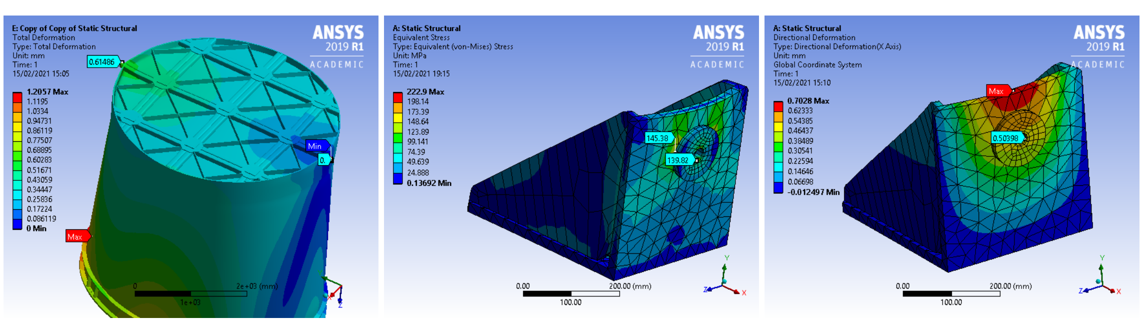

FIG. 48. Results from the analysis showing the displacement near the anchor point on the tank (left) the displacement on the anchor that connects to the floor (center), and the load on the anchor that connects to the floor (right).

TABLE VI. The experimental configurations required for each major measurement in the WCTE.

Measurement	Beam Configuration	Water Configuration
Cherenkov profile measurement	Secondary	Pure or Gd Loaded
Secondary neutron production from protons	Secondary	Gd Loaded
Secondary neutron production from pions	Tertiary	Gd Loaded
Pion scattering and detector response	Tertiary	Pure or Gd Loaded
Energy scale calibration with crossing muons	Secondary	Pure or Gd Loaded
Reconstruction studies for electrons, muons, protons	Secondary	Pure or Gd Loaded
Reconstruction studies for pions	Tertiary	Pure or Gd Loaded

IV. EXPERIMENT RUN PLAN

As discussed in previous sections, we plan to run the WCTE with two different detector configurations: filled with ultra pure water and loaded with Gd. We also plan to run with two different beam configurations, one optimized for tertiary pion production, and one accepting low momentum muons, electrons and protons from the T9 secondary beam line. Table VI shows the required experimental configuration for each of the major physical processes that will be measured in the WCTE. Both secondary and tertiary beam configurations are necessary to make all measurements, while it is possible to make all measurements using only the Gd-loaded water configuration. Restricting the operation to the Gd-loaded configuration would come with the risk that the detector response is not first established with pure water operation. In this section, three different run plans covering the following combinations of experiment configurations will be considered:

- WCTE is operated in all four combinations of beam line and water configurations.
- The pure water configuration is only operated when the beam is in the secondary configuration, and not when the beam is in the tertiary configuration.
- There is no operation in the pure water configuration while in the T9 experimental area. In this case, operation with pure water to collect cosmic ray data while in the assembly area would be considered in order to establish the baseline performance of the detector.

These three run plans will show the range of options considered by the collaboration. The choice of run plan should be made considering the availability of the T9 area during the proposed period of operation.

Here we make preliminary estimates of the run time necessary for each configuration based on the simulations from Section III A. The beam configuration simulated in Section III A produces $\sim$50 tertiary particles of interest per 1×10^6 secondary particles per 50 MeV/c of tertiary momentum. We aim to study a number of reconstructed quantities, including particle misidentification rates as low as 0.1%. To achieve a 5% error on the measured misidentification rates, it is necessary to accumulate approximately 10,000 spills if the secondary rate per spill is 1×10^6. At 3 spills per minute, this corresponds to $\sim$ 3 days of operation. To allow for contingency that covers beam downtime or detector downtime, we schedule two weeks of data-taking for each tertiary beam configuration.

When operating in the secondary beam configuration, it is expected that a longer data-taking period will be necessary since there are additional beam and detector configurations. The secondary beam line momentum acceptance will have to be varied to cover the full momentum range of interest. We also plan to take data with the beam pipe injecting particles at $\sim$5 different radial positions in the WCTE. Each of the beam pipe configuration changes will take $\sim$1/2 day. To account for these configuration changes, we schedule 3 weeks of beam each time we operate in the secondary beam configuration.

The proposed schedule for WCTE operation assuming operation in all configurations of beam and water is shown in Fig. 49. This schedule assumes that the WCTE experiment is assembled outside of the T9 area and initial commissioning of the detector is carried out without water in the assembly area. After the assembly and air-filled commissioning, the detector is moved into the T9 experimental area at the start of this schedule. We schedule two weeks to move the detector into the experimental area and connect services. At the same time, the tertiary beam equipment, including the target, spectrometer, collimator and beam monitors will be set up and the DAQ will be commissioned. After the experiment is set up, one week is scheduled for water filling and circulation. With a water circulation rate of 2 ton/hr, it will be possible to turn over the water volume once per day, sufficient to achieve the required water quality in one week. After the detector is filled with water, one week will be taken to re-commission the detector and take calibration data.

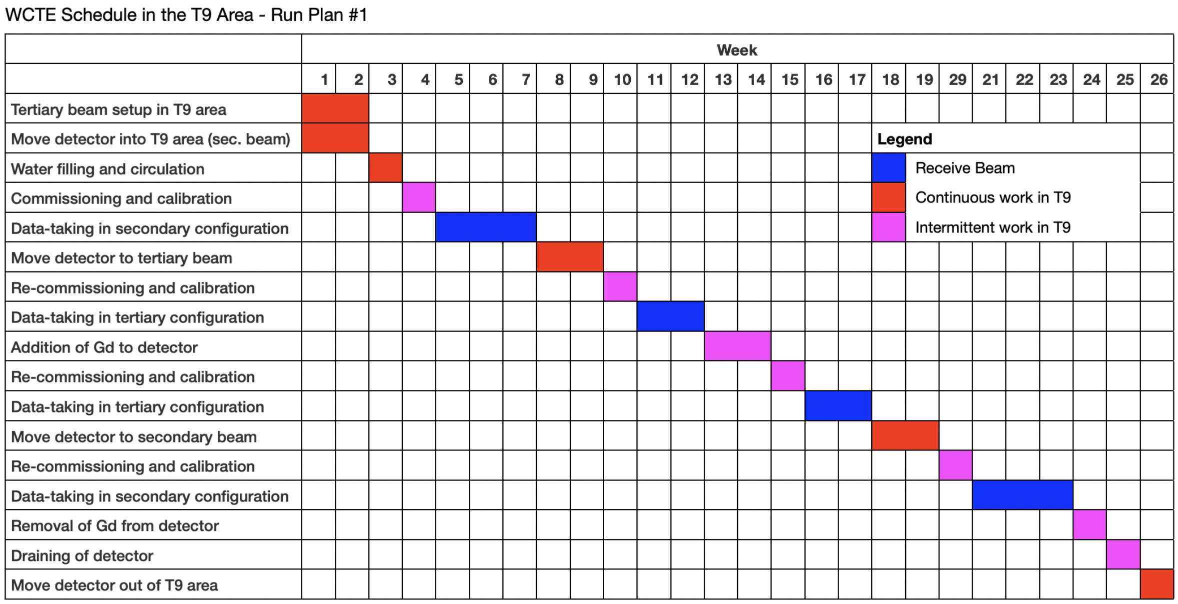

FIG. 49. Proposed schedule for installation and operation of the WCTE experiment in the T9 experimental area with all combinations of beam and water configurations. During the periods marked blue, the experiment will receive beam. During the periods marked red, there will be no beam received, but there will be continuous work in the T9 area. During the periods marked magenta, there will be no beam received, and work in the T9 area will be intermittent.

After commissioning and calibration, the first data taking with ultra-pure water is started. As described above, we schedule two to three weeks of data taking for each experimental configuration, and this time includes contingency for accelerator or detector downtime. We start the operation in the secondary beam configuration since this is the beam configuration in which we will deploy the beam pipe. By starting in this configuration, we can deploy the beam pipe during the water filling phase just after the water level reaches the beam pipe vertical height. This minimizes the chance of a significant water leak during the beam pipe deployment since tank is not fully filled at that time.

Since the cost to add and remove $Gd_2(SO_4)_3$ to the detector is significant, we propose to have a single phase of operation with $Gd_2(SO_4)_3$. Since we take this approach, the second detector operation phase is in the tertiary configuration with ultra-pure water. We schedule two weeks to move the detector into the tertiary configuration since this requires disconnecting and reconnecting the water system. We don't plan to drain the detector before moving it. After moving the detector, we will take another week to re-commission and re-calibrate the detector, followed by two weeks of data taking.

After the ultra-pure water data taking is complete, we will fill the detector with 0.2% $Gd_2(SO_4)_3$, which is scheduled to take place over two weeks. This period is expected to require intermittent access to the experimental area as the $Gd_2(SO_4)_3$ is gradually added and the detector response is evaluated. After the $Gd_2(SO_4)_3$ loading, the schedule for re-commissioning, re-calibration, data taking and moving the detector will repeat.

After operation in each phase is complete, the $Gd_2(SO_4)_3$ will be removed from the water and the water will be drained from the tank. After this, the WCTE detector can be moved out of the T9 experimental area.

Alternative schedules for the run plan that either exclude the pure water operation in the tertiary beam configuration, or exclude the pure water operation in T9 all together, are shown in Fig. 50 and Fig. 51, respectively. These run plans reduce the expected operation time in the T9 area to 20 or 16 weeks, from 26 weeks for the case where data is taken in all possible configurations. The choice of run plan will be made considering all necessary factors, including the availability of the T9 experimental area.

V. SCHEDULE

The schedule for the WCTE, assuming availability of the beam area is shown in Fig. 52. At this time, development and production of the the mPMT photodetectors is likely to be the critical path in the WCTE. However, the purchasing and construction of other components will depend on approval of the experiment, and the schedule may be delayed if

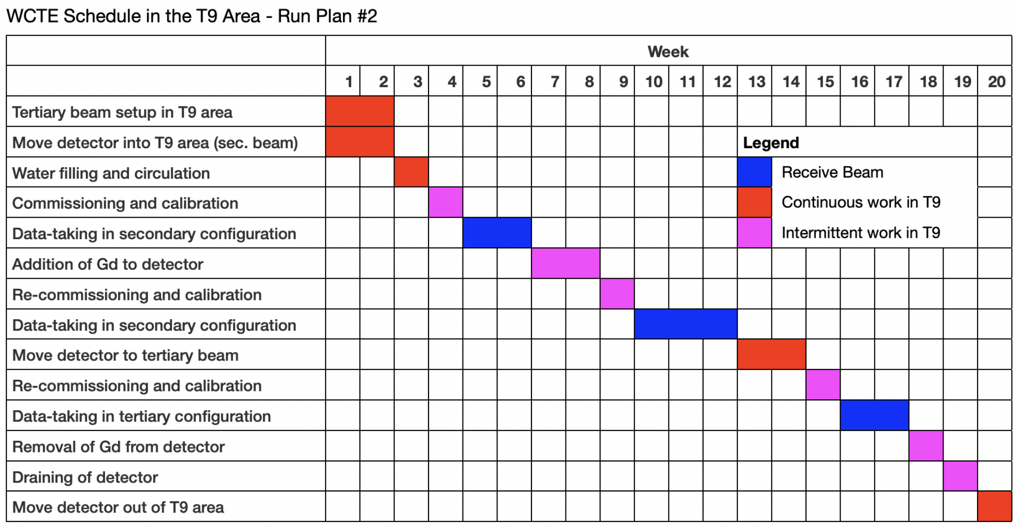

FIG. 50. Proposed schedule for installation and operation of the WCTE experiment in the T9 experimental area with no pure water configuration during the tertiary beam configuration. During the periods marked blue, the experiment will receive beam. During the periods marked red, there will be no beam received, but there will be continuous work in the T9 area. During the periods marked magenta, there will be no beam received, and work in the T9 area will be intermittent.

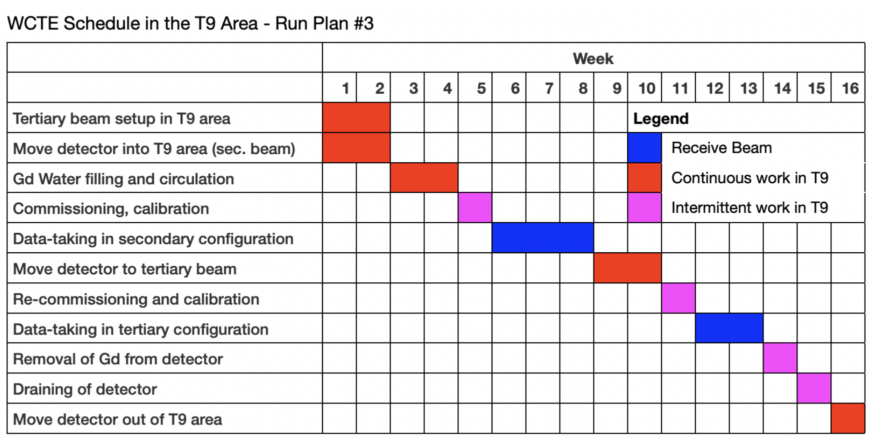

FIG. 51. Proposed schedule for installation and operation of the WCTE experiment in the T9 experimental area with no pure water configuration while operating in T9. During the periods marked blue, the experiment will receive beam. During the periods marked red, there will be no beam received, but there will be continuous work in the T9 area. During the periods marked magenta, there will be no beam received, and work in the T9 area will be intermittent.

approval is delayed. This schedule assumes approval near April 2021, and it can be assumed that the schedule will shift by an equivalent amount for any delays in approval after this time.

The mPMTs are now in the stage of prototyping and design iteration. This stage is expected to extend through the end of calendar year 2021 and accounts for the realized and expected impact of the COVID-19 pandemic. The mPMT production, starting in 2022, will take place at two sites, one in Canada and one in Poland, and a production rate of one module per day per site is expected to be achieved. Given time to ramp up the production capability, the mPMT production should be completed in 6 months, although 8 months is scheduled for contingency.

Other critical components for the detector are the detector tank and mPMT support structure. The tank design is currently being carried out in consultation with CERN experts and is expected to converge by May 2021. It is planned that the detector tank will be fabricated by a company nearby to CERN to allow for ease of shipment to the lab. After arrival of the tank at CERN by May 2022, the beam windows for the tank will be fabricated at CERN, and the tank will be ready for detector construction by November 2022.

The mPMT support structure is planned to be fabricated in India using a modular approach to allow for each of shipment to CERN. The assembly of the support structure modules will start in September 2022, and the support structure parts will be ready in time for the mPMT installation and the detector is assembled.

Other components of the detector will be built in parallel with these key components and be ready for detector assembly by November 2022. It is expected that it will take 6 months to assemble the detector, and it will be ready to move into the experimental area to start data taking by May 2023.

As discussed previously, the run plan for the ultra-pure water configuration and Gd loaded configuration in secondary and tertiary beams will take $\sim 4-6$ months in the T9 experimental area. However, the length of the run plan may be reduced by choosing to limit combination of configurations.

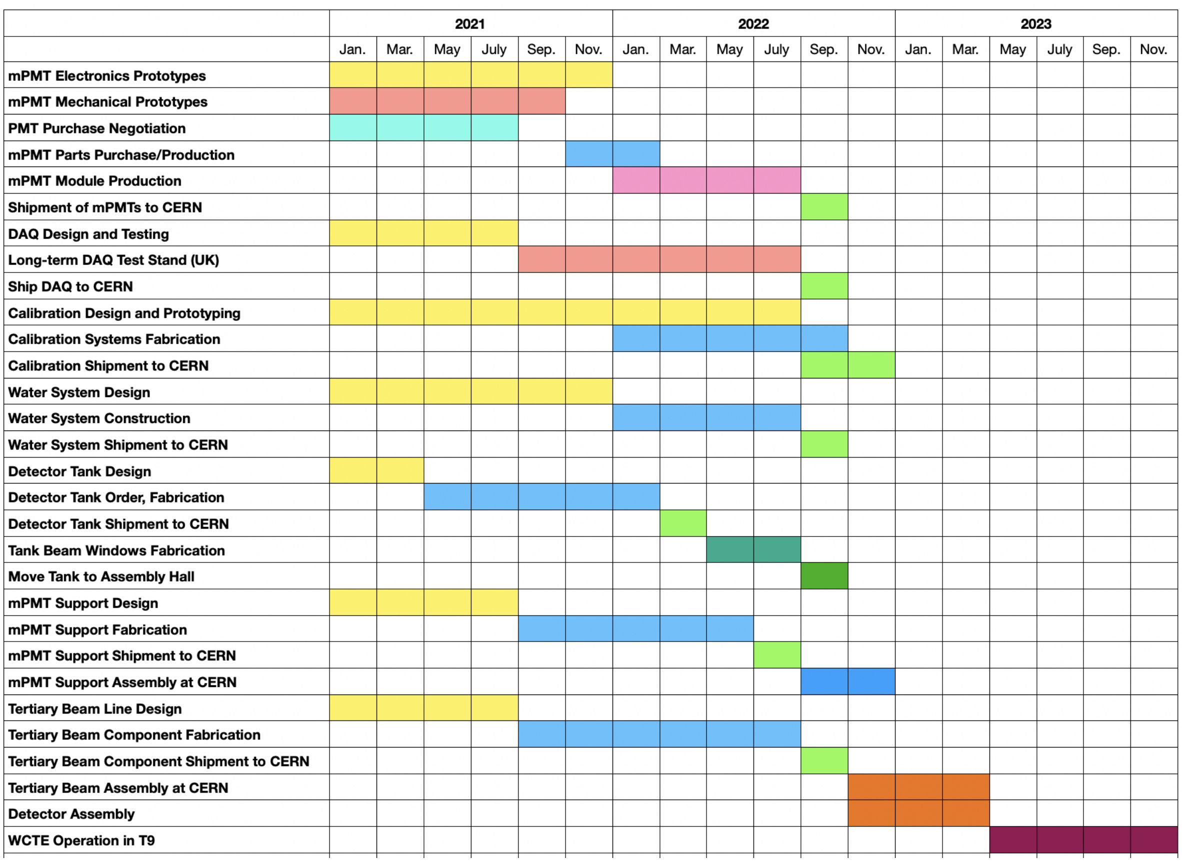

FIG. 52. Schedule of the WCTE. Years are calendar years.

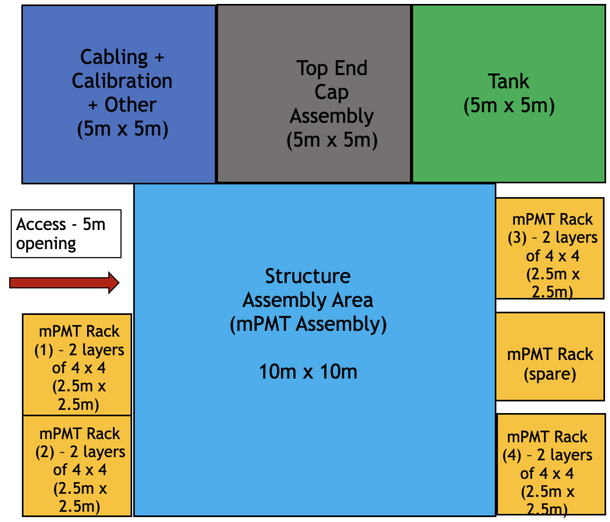

FIG. 53. Floor plan for the WCTE assembly.

VI. REQUEST FOR INFRASTRUCTURE USE AND SUPPORT

The construction and operation of the WCTE at CERN will require use of infrastructure at CERN and support from CERN personnel. Here, we describe the requested infrastructure use and support.

A. Detector assembly area

The WCTE collaboration will need an assembly area where the detector can be assembled before transport to the East Area experimental hall for installation in the T9 beam line. The requirements for this assembly space are:

- 15 m $\times$ 15 m of work space for assembly. The required space is necessary to accommodate the floor plan for assembly shown in Fig. 53.
- An overhead crane with at least 12 m of clearance and 20 ton capacity.
- Door to the assembly hall with dimensions of at least 5 m $\times$ 5 m.
- 6 months use of assembly area, starting as early as November 2022.

Based on these requirements, and in consultation with the Neutrino Platform group, Gargamelle Hall in Building 185 was identified as the candidate assembly area. It has:

- 23 m $\times$ 18 m of work space for assembly.
- An overhead crane with at least 15 m clearance to the hook and a maximum capacity of 40 ton.
- A door with dimensions 5.5 m $\times$ 5.5 m.

The floor plan and pictures of the candidate assembly hall door and overhead crane are shown in Fig. 54.

It may be optimal to ship the multi-PMTs to CERN as they are produced. In this case, the multi-PMTs will start to arrive up to 5 months before the start of the detector assembly. If we take this approach, we will require a 50 m^2 area to store the multi-PMTs before assembly starts.

B. Support for component shipping and receiving

Many of the WCTE components will be built at the locations of WCTE collaborators and shipped to CERN. We request CERN administrative support to arrange the shipment of components to CERN. This may include the shipment of large parts, such as the tank or support structure with maximum dimensions of $\sim$4 m, by road from the port or local fabricator. If this shipment by road requires any special permits, we request CERN administrative support to obtain the permits.

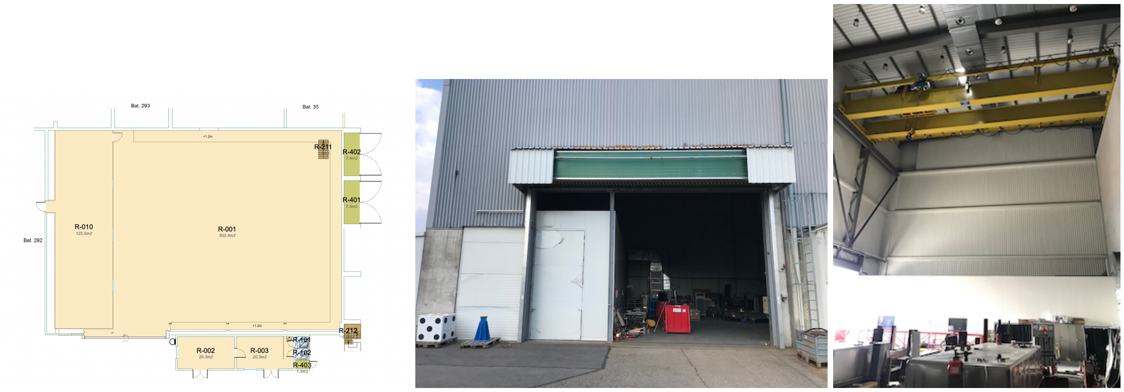

FIG. 54. Floor plan of the Gargamelle Hall assembly area (left), picture of the door to the assembly area (middle) and picture of the overhead crane (right).

C. Support during assembly

The assembly of the detector will require regular use of the overhead crane to lift the support structure parts, lift multi-PMTs into place in the support structure, and to lift the support structure into the detector tank. The experiment will require a crane operator during a significant fraction of the assembly work. In order to carry out the assembly work, the experiment will also require a foreman from the Neutrino Platform to supervise.

The detector support structure and tank will be lifted by the overhead crane during installation and moving. In order to minimize horizontal forces, a lifting beam with four points and a diagonal spacing of 4 m will be necessary. We request to use such a lifting beam if one with these dimensions is available at CERN. If the lifting beam is not available we request that CERN purchase one since it will become part of the available infrastructure at CERN.

D. Detector moving to the experimental area

The detector will need to be moved from the assembly area to the experimental area and be installed in the experimental area before operation. This will be done with the multi-PMTs and support structure installed inside the tank, but before the tank is filled with water. We request the support of the transport group to move the detector before and after the experimental run.

E. Water filling

The time necessary to achieve sufficient water quality in the experimental area can be minimized by initially filling the detector with deionized water. We request the use of 50 ton of deionized water to initially fill the detector.

F. Detector moving system

The detector will be moved between the primary and secondary beam lines using the rail system described in Section III J. We request the support from CERN to install and operate the detector moving system. Since this system can become CERN infrastructure after its use by the WCTE experiment, we also request that CERN purchase this system.

G. Water tank procurement and ports

The collaboration plans to purchase the water tank and its lid from local manufacturers. We will request the support of the CERN purchasing office to carry out this purchase using collaborator funds that are in a CERN account. The water tank has two ports and flanges where the beam windows are installed. We request that the machine shop machine these ports and fabricate and install the flanges for the beam windows.

H. Beam line setup

The tertiary beam requires a collimator made from standard iron shield blocks in order to shield against beam-induced backgrounds. We request the use of the necessary shielding blocks and the support for their installation.

The collaborators will install beam line monitors and magnets in the tertiary and secondary beam configurations. We request support from the relevant experts for the installation of these components in the beam line and their alignment and position survey.

I. General engineering support

Collaborators on the WCTE are producing the designs and engineering drawings of the WCTE components and carrying out the simulations to ensure compliance with safety codes. We request support from CERN engineers to check the designs produced by the collaboration in order to ensure that the compliance with safety codes is met.

J. Office Space

Collaborators with be stationed at CERN during the assembly and operation of the WCTE. While much of the work will be in the assembly and experimental area, we will require about 15 desks for WCTE collaborator use during the assembly and operation phases.

---

[1] K. Abe *et al.*, "Hyper-Kamiokande Design Report," 2018.
[2] M. Wascko, "T2k status, results, and plans," June 2018.
[3] S. Bhadra *et al.*, "Proposal for the NuPRISM Experiment in the J-PARC Neutrino Beamline," 2015.
[4] Y. Fukuda *et al.*, "The Super-Kamiokande detector," *Nucl. Instrum. Meth. A*, vol. 501, pp. 418–462, 2003.
[5] K. Abe *et al.*, "The T2K Experiment," *Nucl. Instrum. Meth. A*, vol. 659, pp. 106–135, 2011.
[6] Y. Fukuda *et al.*, "Evidence for oscillation of atmospheric neutrinos," *Phys. Rev. Lett.*, vol. 81, pp. 1562–1567, 1998.
[7] K. Abe *et al.*, "Observation of Electron Neutrino Appearance in a Muon Neutrino Beam," *Phys. Rev. Lett.*, vol. 112, p. 061802, 2014.
[8] Y. Nakajima, "Recent results and future prospects from super-kamiokande." Neutrino 2020, 2020.
[9] L. Labarga, "The SuperK-gadolinium project," *PoS*, vol. EPS-HEP2017, p. 118, 2018.
[10] K. Abe *et al.*, "Characterization of nuclear effects in muon-neutrino scattering on hydrocarbon with a measurement of final-state kinematics and correlations in charged-current pionless interactions at T2K," *Phys. Rev. D*, vol. 98, no. 3, p. 032003, 2018.
[11] T. Towstego, "Development of a multi-ring sample at the T2K far detector," June 2020.
[12] E. S. P. Guerra, *Measurement of Pion-Carbon Cross Sections at DUET and Measurement of Neutrino Oscillation Parameters at the T2K Experiment*. PhD thesis, York University, 2018.
[13] E. Baussan *et al.*, "A very intense neutrino super beam experiment for leptonic CP violation discovery based on the European spallation source linac," *Nucl. Phys.*, vol. B885, pp. 127–149, 2014.
[14] M. Dracos, "The European Spallation Source Neutrino Super Beam Design Study," p. TUPML068, 2018. [J. Phys. Conf. Ser.1067,no.4,042001(2018)].
[15] T. Akaishi *et al.*, "EMPHATIC: A Proposed Experiment to Measure Hadron Scattering and Production Cross Sections for Improved Neutrino Flux Predictions," 2019.
[16] M. Tabata, "Transparent tiles of silica aerogels for high-energy physics," 2019.
[17] S. Adrián-Martínez *et al.*, "Letter of intent for KM3net 2.0," *Journal of Physics G: Nuclear and Particle Physics*, vol. 43, p. 084001, jun 2016.
[18] K. Abe *et al.*, "Calibration of the Super-Kamiokande Detector," *Nucl. Instrum. Meth.*, vol. A737, pp. 253–272, 2014.
[19] B. Moffat, R. Ford, F. Duncan, K. Graham, A. Hallin, C. Hearns, J. Maneira, P. Skensved, and D. Grant, "Optical calibration hardware for the sudbury neutrino observatory," *Nuclear Instruments and Methods in Physics Research Section A: Accelerators, Spectrometers, Detectors and Associated Equipment*, vol. 554, no. 1, pp. 255 – 265, 2005.
[20] Z. Petriw, *An Underwater Six-Camera Array for Monitoring and Position Measurements in SNO+*. PhD thesis, University of Alberta, 2012.
[21] L. Marti *et al.*, "Evaluation of Gadolinium's Action on Water Cherenkov Detector Systems with EGADS," *Nucl. Instrum. Meth.*, vol. A959, p. 163549, 2020.
[22] M. Yeh, S. Hans, W. Beriguete, R. Rosero, L. Hu, R. L. Hahn, M. V. Diwan, D. E. Jaffe, S. H. Kettell, and L. Littenberg, "A new water-based liquid scintillator and potential applications," *Nucl. Instrum. Meth.*, vol. A660, pp. 51–56, 2011.
[23] L. J. Bignell *et al.*, "Characterization and Modeling of a Water-based Liquid Scintillator," *JINST*, vol. 10, no. 12, p. P12009, 2015.
[24] J. R. Alonso *et al.*, "Advanced Scintillator Detector Concept (ASDC): A Concept Paper on the Physics Potential of Water-Based Liquid Scintillator," 2014.

Appendix A: Potential Future Uses of WCTE Apparatus

1. Water-based Liquid Scintillator

A limitation of water Cherenkov detectors is the inability to detect particles with velocity below the threshold for Cherenkov radiation production. If scintillator can be added to the water, the scintillation light can be used to detect particles below Cherenkov threshold, leading to potential improvements in the energy reconstruction and classification of neutrino interaction events. Significant development of water/scintillator mixtures has been made [22, 23], and the technology is considered for proposed future experiments [24]. The experimental apparatus of the WCTE may find future use as a platform for testing the WbLS technology.

A challenge of potential WbLS detectors is the separate identification of scintillation and Cherenkov light. To address this challenge, photodetectors that enhance the capability to separate scintillation and Cherenkov light in time and wavelength are being developed. One option, the dichroicon photon detector is described here.

2. Dichroicon Wavelength-Separating Cones

When using Water-based Liquid Scintillator (WbLS), the ability to separate Cherenkov and scintillation light can substantially enhance the information extracted from each light source. One method for separating these light sources at the hardware level is the Dichroicon, which is a Dichroic Winston cone that reflects the longer-wavelength portion of the Cherenkov spectrum toward a central red-sensitive photodetector, and allows the shorter-wavelength scintillation light to pass through the cone to a blue-sensitive photonsensor, and shown in Figure 55.

The wavelength distributions of Cherenkov light, PPO, and PTP are shown in Figure 55. By using a Winston cone with a dichroic filter at 450 nm, only the long-wavelength portion of the Cherenkov spectrum is directed toward a central PMT region that accepts wavelengths above 450 nm, which then provides a high-purity measurement of the direction-sensitive Cherenkov light signal. The light that passes through the Winston cone constains nearly all of the scintillation light, as well as the low-wavelength portion of the Cherenkov light, such that nearly all of the photons are still collected to preserve energy resolution for low-energy signals.

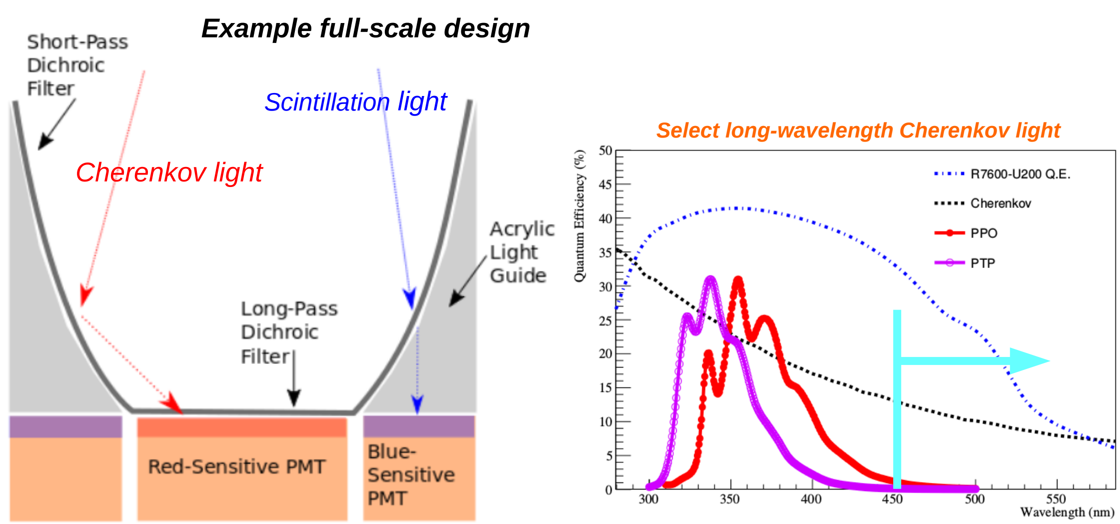

FIG. 55. The left figure shows a schematic of the Dichroicon, and the right figure shows the wavelength distribution of Cherenkov light, POP, and PTP.

Several dichroicons can be deployed in the WCTE to study the separation and collection properties of these devices. Many of the performance metrics can be determined in the pure water phase of the experiment, since Cherenkov photons will be found in high- and low-wavelength sensitive regions. Additional studies in the WbLS phase are needed to study the efficiency for excluding scintillation light in the central Cherenkov-sensitive region.

Appendix B: Tertiary Beam Rates

TABLE VII. Tertiary particle rates between 0.2 GeV/c and 1.2 GeV/c for for 10^6 secondary beam protons at 12 GeV/c.

p [GeV/c]	e^-	e^+	π^+	π^-	p
$0.00-0.05$	0.0	0.0	0.0	0.0	0.0
$0.05-0.10$	0.5	2.5	0.0	0.0	0.0
$0.10-0.15$	9.0	16.0	0.0	0.5	0.0
$0.15-0.20$	19.0	24.0	3.5	5.0	0.0
$0.20-0.25$	16.5	21.5	16.5	13.5	0.0
$0.25-0.30$	13.5	20.5	37.0	27.5	2.5
$0.30-0.35$	15.0	15.5	42.0	42.5	18.5
$0.35-0.40$	11.5	13.0	64.5	46.0	20.0
$0.40-0.45$	11.0	8.0	59.5	61.5	53.5
$0.45-0.50$	8.0	11.5	85.0	70.0	58.0
$0.50-0.55$	7.5	9	85.5	78.0	83.0
$0.55-0.60$	6.5	8.5	81.5	73.5	91.5
$0.60-0.65$	2.5	4.5	90.0	74.0	98.5
$0.65-0.70$	4.0	5.5	85.0	76.5	116.0
$0.70-0.75$	4.0	6.0	73.5	67.5	144.0
$0.75-0.80$	2.0	1.5	75.5	63.0	119.0
$0.80-0.85$	2.5	2.5	66.5	62.5	109.0
$0.85-0.90$	2.0	2.0	59.0	48.5	103.0
$0.90-0.95$	1.0	0.5	50.5	56.0	92.5
$0.95-1.00$	1.5	2.5	47.0	43.5	99
$1.00-1.05$	1.0	2.5	52.5	38.0	84.0
$1.05-1.10$	1.5	0.5	37.5	39.0	71.0
$1.10-1.15$	1.0	1.0	39.0	31.0	72.0
$1.15-1.20$	2.0	1.5	42.0	35.0	67.0

TABLE VIII. Gamma ray background rates in bins of momentum for different tertiary beam particles. The rates are shown as the number of gamma-rays per the number of tertiary beam particles.

	Tertiary beam				
p [MeV/c]	e^-	e^+	π^+	π^-	p
$0-10$	2.7893	2.6406	0.3636	0.3392	0.3405
$10-20$	0.6252	0.6081	0.0419	0.0324	0.04
$20-30$	0.3437	0.2487	0.0129	0.0118	0.0131
$30-40$	0.209	0.1576	0.0046	0.0044	0.0055
$40-50$	0.1295	0.1146	0.0039	0.0018	0.0048
$50-100$	0.3333	0.2682	0.0059	0.0048	0.0068
$100-150$	0.1019	0.1029	0.0017	0.0009	0.0025
$150-200$	0.0484	0.0573	0.0005	0.0007	0.0016
$200-250$	0.0242	0.0352	0.0012	0.0004	0.0007
$250-300$	0.019	0.0221	0.0007	0.0004	0.0011
$300-350$	0.0069	0.0065	0.0005	0.0006	0.0005
$350-400$	0.0069	0.0052	0.0003	0	0.0002
$400-450$	0.0052	0.0039	0.0005	0.0006	0.0003
$450-500$	0.0017	0.0065	0.0002	0	0.0002
> 500	> 0.0242	0.0104	0.0007	0.0013	0.0011

TABLE IX. Neutron background rates in bins of momentum and kinetic energy for different tertiary beam particles. The rates are shown as the number of neutrons per the number of tertiary beam particles.

		Tertiary beam				
p [MeV/c]	KE [MeV]	e^-	e^+	π^+	π^-	p
$0-10$	$0.0-0.05$	0.1399	0.1510	0.1439	0.1380	0.1225
$10-20$	$0.05-0.21$	0.0415	0.0573	0.0597	0.0614	0.0520
$20-30$	$0.21-0.48$	0.0380	0.0326	0.0337	0.0389	0.0378
$30-40$	$0.48-0.85$	0.0259	0.0391	0.0336	0.0343	0.0320
$40-50$	$0.85-1.33$	0.0173	0.0195	0.0236	0.0216	0.0222
$50-100$	$1.33-5.31$	0.0587	0.0430	0.0622	0.0630	0.0556
$100-150$	$5.31-11.90$	0.0173	0.0169	0.0178	0.0203	0.0161
$150-200$	$11.90-21.05$	0.0104	0.0091	0.0105	0.0114	0.0123
$200-250$	$21.05-32.69$	0.0069	0.0182	0.0085	0.0083	0.0081
$250-300$	$32.69-46.73$	0.0052	0.0104	0.0097	0.0098	0.0071
$300-350$	$46.73-63.07$	0.0086	0.0078	0.0085	0.0087	0.0121
$350-400$	$63.07-81.60$	0.0138	0.0117	0.0075	0.0074	0.0073
$400-450$	$81.60-102.20$	0.0086	0.0091	0.0075	0.0085	0.0099
$450-500$	$102.20-124.76$	0.0052	0.0091	0.0069	0.0070	0.0069
>500	>124.76	0.0294	0.0365	0.0378	0.0359	0.038

TABLE X. Electron background rates in bins of momentum and kinetic energy for different tertiary beam particles. The rates are shown as the number of electrons per the number of tertiary beam particles.

		Tertiary beam				
p [MeV/c]	KE [MeV]	e^-	e^+	π^+	π^-	p
$0-10$	$0.0-9.50$	0.0587	0.0677	0.0322	0.028	0.0218
$10-20$	$9.50-19.5$	0.0138	0.013	0.0029	0.0026	0.0018
$20-30$	$19.50-29.49$	0.0173	0.0182	0.0003	0.0002	0.0008
$30-40$	$29.49-39.49$	0.0035	0.0091	0.0005	0.0011	0.0001
$40-50$	$39.49-49.49$	0.0017	0.0026	0.0003	0.0002	0.0002
$50-100$	$49.49-99.49$	0.0052	0.0117	0.0003	0.0004	0.0004
$100-150$	$99.49-149.49$	0.0017	0.0065	0	0	0.0002
$150-200$	$149.49-199.49$	0	0.0026	0	0	0.0001
$200-250$	$199.49-249.49$	0.0017	0	0.0002	0	0.0001
$250-300$	$249.49-299.49$	0	0.0026	0.0002	0	0
$300-350$	$299.49-349.49$	0	0.0039	0	0	0
$350-400$	$349.49-399.49$	0	0	0	0	0
$400-450$	$399.49-449.49$	0	0	0	0	0
$450-500$	$449.49-499.49$	0	0	0	0	0
>500	>124.76	0	0	0	0	0.0001